Microglia regulate developmental transitions in synaptic plasticity rules in the medial prefrontal cortex

Mio Tajiri[1, 3], Hidefumi Omi[1, 3], Airi Inoue[1], Hayato Etani[1], Takeshi Sawada[1], Yusuke Iino[1], Sho Yagishita[1, 2]*

[1] Laboratory of Structural Physiology, Center for Disease Biology and Integrative Medicine, Graduate School of Medicine, The University of Tokyo, Tokyo, Japan

[2] International Research Center for Neurointelligence (WPI-IRCN), UTIAS, The University of Tokyo, Tokyo, Japan

[3] These authors contributed equally to this work.

* Corresponding author: yagishita-tky@umin.ac.jp

Abstract

Synaptic plasticity is governed by rules that determine how patterns of neural activity are converted into changes in synaptic weights. While neocortical plasticity rules appear to shift from Hebbian to three-factor forms during development, the cellular mechanisms underlying this transition remain unclear. Here, we show that microglia mediate the developmental transition of plasticity rules at individual dendritic spines in the medial prefrontal cortex (mPFC) during juvenile-to-adolescent maturation. After maturation, microglia suppressed Hebbian activity–induced spine enlargement via a humoral factor. This suppression was relieved by noradrenaline through microglia-intrinsic cAMP signaling, thereby enabling a three-factor rule for gating plasticity. The adolescent mPFC required three-factor plasticity signaling for the acquisition of socially learned fear. Local microglial ablation enhanced learning efficiency but also altered pain sensitivity in a learning-dependent manner, suggesting that microglial suppression safeguards pre-existing emotional circuits. Together, these findings identify microglia as critical regulators of developmental plasticity-rule transitions in the mPFC.

Main

Synaptic plasticity is the fundamental neural mechanism for learning (1, 2), which is controlled by "rules" that determine how patterns of neural activity are converted into changes in synaptic weights (3–10). In the neocortex, these rules appear to shift across maturation (5, 11–14). During childhood, neocortical circuits can remodel according to the Hebbian rule, strengthening synapses through coincident pre- and postsynaptic activity driven by glutamate (5, 15–18). From adolescence onward, however, Hebbian weight updates become less effective (14, 18–22), and plasticity increasingly depends on neuromodulatory contexts involving reward or punishment (23–29). The requirement for neuromodulators such as monoamines as a third factor, in addition to the two factors of pre- and postsynaptic activity, is known as the three-factor rule (7–9). This rule enables neural circuits to selectively update synaptic weights based on behaviorally relevant feedback. As excessive plasticity can destabilize established circuits (30, 31), this shift may stabilize existing representations while permitting updates only in select contexts, including emotionally salient ones, thereby contributing to the neocortical capacity for long-term information storage (30–33). Although this framework highlights both reduced Hebbian plasticity and increased neuromodulator-dependent mechanisms as central to the shift in synaptic rules in the neocortex, the exact cellular mechanisms are not well understood.

At excitatory glutamatergic synapses, dendritic spines function as the basic units for synaptic weight updating (34, 35). In the neocortex, spine volume reflects AMPA receptor content (36, 37) and learning induces input-specific structural long-term potentiation (sLTP) of dendritic spines (38–40). In *ex vivo* studies using hippocampal slices, the Hebbian pairing of glutamatergic

input with postsynaptic spikes reliably induces sLTP (41–43). In contrast, glutamatergic stimulation induces far less prominent sLTP in the mature neocortex (44), suggesting the necessity of a three-factor rule. Consistent with this idea, neuromodulators such as noradrenaline (NA) enhance spine plasticity in vivo (45), supporting a role for neuromodulatory reinforcement in sLTP alongside concurrent glutamatergic synaptic activity during learning (38–40). Despite extensive work on the role of sLTP in neocortical learning, it remains unclear how Hebbian pairing-induced sLTP is suppressed in the mature neocortex and how this suppression interacts with neuromodulator-driven facilitation.

Both neuron-intrinsic maturation and glial mechanisms have been proposed to developmentally regulate plasticity, potentially contributing to Hebbian plasticity suppression. Neurons may raise the threshold for glutamatergic induction of plasticity (12, 18, 46), making neuromodulatory input increasingly necessary. More recent studies highlight glial roles in synaptic regulation. In particular, microglia regulate synapse number and spine turnover during developmental maturation (47–50) and respond to noradrenergic signals (51, 52) to influence synaptic function (52). However, it remains unclear whether microglia actively participate in defining rules for weight updates at the moment neural activity occurs, or instead modulate synaptic changes hours later, given the limited temporal resolution of current *in vivo* studies. Furthermore, conflicting findings report that microglia can either enhance or restrict day-scale structural remodeling (47, 49, 52–57), leaving their contribution to plasticity rules unresolved. Within the neocortex, the medial prefrontal cortex (mPFC), a key region for neuromodulator-dependent emotional learning (26, 58–62), undergoes synaptic maturation during adolescence with microglial involvement (63). Thus, the mPFC provides a critical site to investigate whether microglia contribute to the

adolescent shift from Hebbian to three-factor learning rules, thereby helping establish emotional learning while maintaining pre-existing circuits.

In this study, we paired two-photon glutamate uncaging with action potential firing to impose a Hebbian pairing activity pattern on individual dendritic spines while simultaneously visualizing those spines and nearby microglia in acute mPFC slices. We observed a developmental decline in Hebbian pairing-induced sLTP and identified microglia as key mediators of this suppression, which depended on humoral signaling rather than process surveillance. We then tested whether sLTP could be induced by a three-factor rule by introducing neuromodulatory signals of NA, and found that NA relieved microglial suppression to gate sLTP through microglia-intrinsic signaling pathways. To examine the behavioral relevance of this plasticity mechanism, we used social fear learning (62, 64–68), which is rapidly acquired within a day and involves mPFC remodeling during learning (69). Finally, we asked whether microglia-mediated suppression of plasticity contributes to maintaining the functional integrity of emotional circuits during learning.

Microglial suppression of spine enlargement during development

We first characterized neocortical sLTP induced by the Hebbian pattern of coincident pre- and postsynaptic activity in adolescent and juvenile mice, both in the presence and absence of microglia. To ablate microglia, we locally injected clodronate into the mPFC and confirmed nearly 90% ablation across a broad region of the mPFC 1–2 days after injection (Supplementary Figure 1A−C) (53). To visualize microglia in acute slices, we generated double-transgenic mice carrying a microglia-specific Cre driver allele, Tmem119-CreERT2, which preserves endogenous

transmembrane protein 119 (Tmem119) gene expression through a P2A sequence (70), along with a Cre-dependent tdTomato reporter allele (Ai14), achieving more than 99% labeling in the mPFC (Figure 1A, Supplementary Figure 1D−G).

Coronal acute slices containing the mPFC were prepared from adolescent (5 to 7 weeks) and juvenile (2 to 3 weeks of age) mice. Layer 5 pyramidal neurons in the mPFC were subjected to whole-cell recordings and perfused with Alexa 488 to visualize dendritic spines using two-photon microscopy (980 nm) (Figure 1B−D, Supplementary Figure 1H,I). Small spines located on the first to third branches of the apical dendrites were selected for plasticity induction. Caged glutamate (4 mM CDNI-Glu) was locally applied through a pressure pipette, and a two-photon laser was directed to the tip of the spine head (720 nm). Uncaging stimulation of 3 or 4 spines, which elicited excitatory postsynaptic potential, was paired with action potentials by current injections following a spike-timing dependent plasticity (STDP) stimulation protocol (Figure 1E, Supplementary Figure 1J) (71, 72).

The STDP stimulation caused a transient increase in spine volume that returned to baseline by 50 minutes in adolescent mice (Figure 1F; n = 5 dendrites, including 19 spines from 4 mice), but it was sustained by 50 minutes in juvenile mice (2−3 weeks of age) (Figure 1G; n = 7 dendrites, including 28 spines from 3 mice). Ablation of microglia restored sustained sLTP in adolescent mice to levels similar to those in juveniles, while having little effect in the juvenile group (Figure 1H−K; clodronate in adolescent, n = 7 dendrites, including 27 spines from 5 mice; clodronate in juvenile, n = 6 dendrites, including 20 spines from 3 mice). Neighboring spines remained stable, indicating that microglial ablation preserved stimulation-specific sLTP (Figure 1H, I). A second

microglia-ablating compound, PLX3397 (73), replicated the effect of clodronate in adolescent mice (Supplementary Figure 1K−M; 6 dendrites, including 23 spines from 3 mice).

Plotting spine volume changes against age revealed an age-dependent decline in sLTP in the presence of microglia (Figure 1L; w/o clodronate, data shown in Figure 1F,G, and additional data from mice aged 3−5 weeks; n = 16 dendrites, including 64 spines from 12 mice in total). In contrast, this decline was not observed when microglia were absent (w/ clodronate, data shown in Figure 1H,I; n = 13 dendrites, including 47 spines from 8 mice in total). Given the established correlation between dendritic spine volume and glutamate sensitivity in the neocortex (36, 37), these findings align with the previously reported developmental decline in LTP (14, 18–20) during the transition from juvenile to adolescent stages. Our data further suggest that microglia acquire a suppressive role during this developmental window, whereas pyramidal neurons maintain an intrinsic capacity for sLTP.

The absence of sLTP in adolescents might depend on stimulation strength. To examine this possibility, we performed plasticity induction in magnesium-free extracellular solution (Supplementary Figure 2A), which evokes a strong Ca^{2+} influx upon glutamate uncaging without requiring action potentials, a widely adopted method for sLTP induction in the hippocampus (34, 74, 75). Even under this magnesium-free condition, glutamate uncaging (0.6 ms pulse, 5 Hz, 300 times) failed to induce sLTP in slices from adolescent mice (Supplementary Figure 2B,C; 7 dendrites, including 32 spines from 5 mice). In contrast, sLTP was induced in microglia-ablated slices (Supplementary Figure 2B,D,E; 5 dendrites, including 18 spines from 4 mice), replicating the results obtained with STDP stimulation (Figure 1J).

The same magnesium-free protocol was sufficient to induce sLTP in the spines of spiny-projection neurons in the nucleus accumbens, which is located in the same coronal section as the mPFC in adolescent mice (Supplementary Figure 2F,G; 5 dendrites, including 19 spines from 4 mice). Given that the STDP stimulation protocol in the nucleus accumbens requires G_s activation through dopamine or adenosine for sLTP induction (71, 72), the ability of the magnesium-free condition to induce sLTP supports the view that this stimulation protocol is stronger than the STDP protocol. In contrast to the mPFC of adolescent mice, microglial ablation did not further promote sLTP in the nucleus accumbens (Figure 1M, Supplementary Figure 2F,H; 5 dendrites, including 19 spines from 4 mice), indicating regional differences in the microglial suppression of plasticity.

Acute slice preparation may alter microglial status (76). A previous study reported a gradual increase in tissue ATP levels over 5 hours after slice preparation, leading to morphological changes in microglia through receptors such as $P2Y_{12}$ receptors (76). Because we observed microglia ablation effects only in the adolescent mPFC, it is possible that microglia in the adolescent PFC are more sensitive to ATP-related alterations than those in the nucleus accumbens or in the juvenile PFC. We therefore reanalysed the STDP stimulation results by dividing the data into the first 2.5 hours and the later period. However, we found no significant difference between these two time windows (Supplementary Figure 3A). Additionally, inhibition of $P2Y_{12}$ receptors did not induce plasticity with STDP stimulation alone (Supplementary Figure 3B; 7 dendrites, including 27 spines from 5 mice). These observations indicate that alterations in

157 microglia caused by acute slice preparation cannot by themselves account for the suppressive
158 effect observed in the adolescent mPFC.

159 Together, these results indicate that during the transition from juvenile to adolescent stages,
160 microglia in the mPFC acquire a suppressive function that limits Hebbian pairing induction of
161 sLTP, whereas pyramidal neurons retain their intrinsic capacity for plasticity.

162 Downstream signaling of microglial suppression

163 Having established that microglia suppress sLTP during adolescence, we next asked how this
164 suppression is implemented at the cellular and molecular levels, either through direct microglial
165 contact with spines or through the release of humoral factors (49, 54, 77–84). If suppression
166 requires physical contact, STDP stimulation should recruit microglial processes to the vicinity of
167 stimulated spines. In acute slices from Tmem119-CreERT2; Ai14 (Figure 2A), in which more
168 than 99% of microglia express tdTomato (Supplementary Figure 1F), microglial protrusions were
169 dynamically recruited to the site of adenosine triphosphate (ATP) application via a pipette within
170 10 minutes (Figure 2B,C), consistent with the previous report (85). When dendritic spines and
171 microglia were imaged simultaneously, fewer than 25% of spines were located near microglial
172 processes before stimulation (Supplementary Figure 4A−C). Unlike ATP application, STDP
173 stimulation did not recruit the microglial processes to stimulated spines, as assessed by
174 fluorescence intensity (Figure 2C,D) or contact counts (Supplementary Figure 4C). These results
175 therefore do not support a mechanism involving physical contact.

We thus tested whether humoral factors—tumor necrosis factor-α (TNF-α) and interleukin-1β (IL-1β) —previously suggested to suppress LTP in the hippocampus (80–82) and preferentially expressed in the microglia in the neocortex (86–90), would also suppress sLTP in the mPFC. In microglia-ablated slices (Figure 2E), bath applied TNF-α (10 nM, bath) (91), but not IL-1β (1 ng/ml, bath) (81), suppressed STDP-induced sLTP (Figure 2E−G, Supplementary Figure 4D−F; TNF-α, n = 6 dendrites, including 21 spines from 4 mice; IL-1β, n = 6 dendrites, including 21 spines from 4 mice). TNF-α can signal through a soluble form released after cleavage by TNF-α converting enzymes (TACE) or A disintegrin and metalloprotease 17 (ADAM17) (92, 93). Inhibition of TACE/ADAM17 by TAPI-0 (1 μM, bath) allowed sLTP in the presence of microglia (Figure 2H, Supplementary Figure 5G; w/o TAPI-0, n = 8 dendrites, including 31 spines from 4 mice; w/ TAPI-0, n = 6 dendrites, including 17 spines from 5 mice). Another class of TNF-α inhibitor, pomalidomide (100 μM, bath) (94, 95), further supported the involvement of TNF-α signaling (Supplementary Figure 5H; n = 6 dendrites, including 21 spines from 4 mice). Moreover, TNF-α suppressed sLTP even in the juvenile mPFC (Figure 2I, Supplementary Figure 4I; n = 7 dendrites, including 26 spines from 5 mice).

Given that microglia are a major source of TNF-α (88–90), these results suggest that microglial suppression of sLTP involves the humoral action of TNF-α in adolescent mice, potentially reflecting developmental changes in microglial properties (96).

Microglia-mediated actions of NA on spine enlargement

We next tested whether neuromodulatory signals could relieve the microglial suppression under physiological conditions, thereby enabling a three-factor rule for sLTP induction. NA was a strong candidate, given its established role in modulating neocortical synaptic plasticity (13, 27, 97) and its direct effects on microglial function (51, 52). We therefore locally delivered NA (50 μM) via a pressure pipette along with the caged-glutamate, beginning 3−5 minutes before the onset of STDP stimulation to mimic the transient NA release observed *in vivo* (62) (Figure 3A−G). The presence of NA during STDP stimulation enhanced sustained sLTP in the stimulated spines up to 50 minutes (Figure 3B,C,G; STDP only, n = 9 dendrites, including 36 spines from 6 mice; STDP with NA, n = 7 dendrites, including 22 spines from 6 mice; P = 0.028, post hoc Steel's test against STDP after Kruskal–Wallis test against the following experiments shown in Figure 3C−G, Supplementary Figure 5A−H). In contrast, dopamine (50 μM, puff), another catecholamine known to influence spine dynamics *in vivo* (98), did not promote sLTP, unlike its effect in the nucleus accumbens (71) (Figure 3G, Supplementary Figure 5A; n = 6 dendrites, including 24 spines from 4 mice; P = 1.00).

Next, we characterized downstream signaling of NA by pharmacologically perturbing G_s-coupled β adrenergic receptors (ARs), which stimulate cAMP production, and phosphodiesterase (PDE), which degrades cAMP, given that the β-ARs-cAMP-PKA pathway generally facilitates LTP (99, 100). RNA-seq data provide comprehensive information on the cellular distribution of β-ARs in the neocortex (86, 101), showing that β_1- and β_3-ARs are primarily localized to neurons and astrocytes, whereas β_2-ARs are predominantly expressed in

215 microglia. Bath application of ICI118,551 (1 μM, β_2 inverse agonist) blocked NA-enhanced
216 sLTP (Figure 3D,G, Supplementary Figure 5B, n = 6 dendrites, including 23 spines from 3 mice;
217 P = 1.00), whereas metoprolol (1 μM, β_1 inverse agonist) did not (Figure 3D,G, Supplementary
218 Figure 5C, n = 7 dendrites including 28 spines from 5 mice; P = 0.038). Moreover, puff
219 application of clenbuterol (10 μM, a β_2 agonist) reproduced the effect of NA on sLTP (Figure 3E,
220 Supplementary Figure 5D, n = 7 dendrites, including 23 spines from 7 mice; P = 0.028). Among
221 the PDE families, PDE3b is preferentially expressed in microglia (102), whereas PDE4 subtypes
222 are expressed in pyramidal neurons (86). We therefore hypothesized that PDE inhibition could
223 substitute for G_s-coupled receptor stimulation. STDP alone induced sLTP in the presence of
224 cilostamide (1 μM bath, PDE3 inhibitor) (Figure 3F,G, Supplementary Figure 5E; n = 7
225 dendrites, including 27 spines from 5 mice; P = 0.028). In contrast, rolipram (1 μM bath, PDE4
226 inhibitor), at a concentration known to enhance hippocampal LTP (103), did not facilitate sLTP
227 (Figure 3F,G, Supplementary Figure 5F; n = 6 dendrites, including 24 spines from 3 mice; P =
228 0.84). These pharmacological results support the hypothesis that NA-mediated sLTP facilitation
229 involves β_2-adrenergic receptors on microglia.

230 Further pharmacological experiments confirmed that the NA-dependent sLTP was abolished by
231 D-AP5 (50 μM, bath application; NMDA receptor antagonist) (Figure 3G, Supplementary Figure
232 5G; n = 7 dendrites, including 27 spines from 6 mice; P = 0.99) and by PKI (10 μM, a PKA
233 inhibitor, in the intracellular solution) (Figure 3G, Supplementary Figure 5H; n = 6 dendrites,
234 including 23 spines from 4 mice; P = 0.98). We next tested whether expressing the CaMKII
235 inhibitory peptide AIP (autocamtide-2-related inhibitory peptide) prevents sLTP (71, 104). AIP
236 was delivered using an AAV vector under CaMKII promoter (Figure 3H). NA-dependent sLTP

237 was observed in neurons expressing the control vector (Figure 3I, Supplementary Figure 5I; n =
238 6 dendrites, including 24 spines from 6 mice) but was blocked in AIP-expressing neurons
239 (Figure 3I, Supplementary Figure 5J, n = 7 dendrites, including 23 spines from 4 mice). These
240 data indicate that the essential signaling mechanisms underlying sLTP are similar to those
241 described in the hippocampus and striatum (42, 71, 72).

242 Using microglia-specific chemogenetic inhibition of cAMP signaling, we further tested whether
243 microglia mediate the action of NA (Figure 3J). We used double-transgenic mice expressing
244 hM4Di, a $G_{i/o}$-coupled receptor that suppresses cAMP production in a Cre-dependent manner
245 (R26-LSL-hM4Di-mCitrine)(105) under the control of Tmem119-CreERT2 (Figure 3K). This
246 combination has been used in recent studies to modulate microglial functions (106, 107). The
247 R26-LSL-hM4Di-mCitrine line is known to exhibit leak expression, which was observed in 3%
248 of cells in the mPFC (Supplementary Figure 6A−C). After repeated intraperitoneal tamoxifen
249 injections (Supplementary Figure 6D), we confirmed expression of the chemogenetic probe in
250 microglia in fixed slices, along with leak expression in other cell types (Supplementary Figure
251 6E,F).

252 In acute slices, we recorded from pyramidal neurons without detectable mCitrine fluorescence
253 and applied deschloroclozapine (DCZ, 100 nM), a potent hM4Di actuator(108–110) in the bath.
254 We found that the presence of Cre prevented sLTP induction by STDP stimulation with NA
255 (Figure 3L−O; without Cre, n = 6 dendrites, including 24 spines from 3 mice; with Cre, n = 6
256 dendrites, including 24 spines from 4 mice). Importantly, STDP-induced sLTP was fully
257 preserved in non-Cre slices from the same double-transgenic mice (Figure 3C vs. Figure 3M),

258 indicating that leak expression and potential off-target effects of DCZ did not impair plasticity.
259 These results therefore indicate that microglial cAMP signaling mediates the NA-dependent
260 enhancement of spine enlargement.

261 Microglial ablation experiments suggested that TNF-α suppresses plasticity downstream of
262 microglia (Figure 2G, Figure 3J), implying that TNF-α may interfere with the effect of NA on
263 plasticity. Consistent with this idea, TNF-α application reduced NA-enabled sLTP induced by
264 STDP (Figure 3P, Supplementary Figure 6G, w/o TNF-α, n = 6 dendrites, 24 spines from 5 mice;
265 w/ TNF-α, n = 8 dendrites, 31 spines from 5 mice).

266 Collectively, our *ex vivo* experiments demonstrate that microglia play a key role in the
267 developmental transition of plasticity rules from a Hebbian form to a three-factor form for sLTP
268 induction in the mPFC. In this framework, microglia adopt a suppressive role in Hebbian
269 plasticity after maturation through a humoral factor, whereas NA can counteract this suppression
270 via β_2-ARs and cAMP signaling within microglia.

271 NA-dependent plasticity signaling in rapid social learning

272 We next tested whether the three-factor rule governed by the NA-dependent plasticity pathway
273 contributes to social emotional learning using the observational fear learning (OFL) paradigm,
274 which engages the mPFC (64, 65, 69, 111). Pairs of male adolescent mice (6–7 weeks old) were
275 co-housed for 4 days. On day 1, one mouse (the observer) received two foot shocks (0.4 mA, 2 s)
276 in a conditioning chamber (Figure 4A). On day 2, the cage mate (the demonstrator) was placed in
277 the same chamber and exposed to 24 tone–shock pairings (6 kHz tone, 5 s; 0.7 mA shock, 2 s).

Tone and shock presentations elicited transient freezing in observers regardless of demonstrator presence, likely due to novelty, whereas sustained freezing occurred only when observers witnessed their cage mate being shocked (Figure 4B, Supplementary Figure 7A; with demonstrator, n = 8; without, n = 6). On day 3, memory was assessed by presenting the tone alone (6 kHz, 60 s, 3 trials). Observer mice exhibited robust freezing during tone presentation, but only if they had previously witnessed the demonstrator being shocked (Figure 4C, Supplementary Figure 7B). Although female mice also acquired OFL, their freezing responses on day 2 were weaker (Supplementary Figure 7C–F, n = 6). Because day 2 freezing was used as an internal reference for subsequent experiments, females were excluded from further testing.

We then assessed NA dynamics in the mPFC using the GPCR-based fluorescent sensor GRAB-NE_{2m} (112). An AAV expressing GRAB-NE_{2m} under the synapsin promoter was injected into the right mPFC, and fluorescence was recorded through an implanted optical fiber (Figure 4D). As a positive control, direct foot shock elicited a transient fluorescence increase that peaked within seconds and decayed over tens of seconds (Supplementary Figure 7G,H; n = 5 mice), consistent with prior reports (61). During OFL, GRAB-NE_{2m} signals in observer mice increased transiently during the 240-second shock period delivered to demonstrator mice on day 2 (Figure 4E, Supplementary Figure 7I, n = 6 mice), consistent with noradrenergic axon activity patterns (62). In contrast, no signal increase was observed on day 3 during cue-driven recall (Supplementary Figure 7J–L). These results indicate that demonstrator distress evokes a sustained, minute-scale NA response in the mPFC, resembling the timing of NA application in

our slice experiments (Figure 3A,C). Although GRAB-NE_{2m} was expressed in neurons, this volume-transmitted NA signal likely reflects levels accessible to microglia.

To test the role of β_2-ARs in the acquisition of OFL, we bilaterally infused ICI118,551 or ACSF as a vehicle control into the mPFC on day 2 through pre-implanted cannulas (Figure 4F). Infusion of ICI118,551 did not alter freezing response during conditioning but subsequently inhibited freezing on day 3 (Figure 4G,H, Supplementary Figure 7M,N, Vehicle, n = 7 mice; ICI118,551, n = 6 mice). Because freezing during conditioning typically correlates with memory strength (67), this dissociation suggests that β_2-AR blockade selectively impaired memory formation rather than fear expression. Together with reports that non-selective β-AR antagonists suppress vicarious fear responses (62), these findings indicate that β_2-AR in the mPFC preferentially contributes to memory formation, whereas β_1-AR may play a more direct role in fear expression.

Given that AIP prevented sLTP induction, we bilaterally expressed AIP in the mPFC and anterior cingulate cortex (ACC) (Figure 4I, Supplementary Figure 8A). This manipulation did not alter freezing during conditioning on day 2 (Figure 4J, Supplementary Figure 8B, mCherry, n = 10 mice; AIP, n = 8 mice) but impaired freezing on day 3 test (Figure 4K, Supplementary Figure 8C), consistent with the effects observed in the β_2 blockade experiment.

These results indicate that the NA-dependent plasticity pathway in the mPFC is required for the rapid formation of social fear learning in adolescent male mice, supporting a role for the three-factor rule in plasticity induction during emotional learning.

Microglial role in rapid social learning

As microglia suppress sLTP induction in the adolescent mPFC (Figure 1J), we predicted that microglial ablation in the mPFC would enhance the acquisition of observational fear learning (OFL). Clodronate was unilaterally injected into the right mPFC on day 0 through a glass pipette, and its spread extended into the anterior ACC by the following day (Figure 5A–C, Supplementary Figure 9A). To avoid ceiling effects during OFL, demonstrator mice received lower-intensity foot shocks (0.2 mA) with fewer repetitions (12 trials) on day 2 (Figure 5A). Under this subthreshold protocol, control observer mice showed freezing during conditioning (Figure 5D, Supplementary Figure 9B) but showed only modest freezing to the tone during testing on day 3 (Figure 5E, Supplementary Figure 9C). Microglial ablation did not affect freezing during conditioning (Figure 5D, Supplementary Figure 9B; Vehicle, $n = 7$ mice; Clodronate, $n = 6$ mice) but significantly increased freezing on day 3 (Figure 5E, Supplementary Figure 9C). These results support the interpretation that microglial ablation facilitates learning rather than simply enhancing threat sensitivity.

To examine the functional role of microglial suppression of sLTP, we next asked whether enhanced plasticity in the absence of microglia leads to the recruitment of task-irrelevant, emotion-related circuits. Pain is an emotional function partly regulated by the mPFC, including the ACC, where synaptic potentiation modulates sensitivity (113, 114). Notably, some neurons in this region encode overlapping representations of pain and vicarious fear (68), suggesting that precise plasticity control is required to update vicarious fear memories without disrupting pain-related processing. We therefore hypothesized that OFL in the absence of microglia could

alter pain sensitivity in a learning-dependent manner. To assess pain sensitivity, we used the thermal place preference (TPP) test (66), in which mice were allowed to freely explore two plates maintained at different temperatures. Avoidance of the warmer plate serves as a readout of thermal nociception. Control mice showed a modest tendency to avoid 40 °C plate, no discrimination between identical 30 °C plates, and consistent avoidance of the 50 °C plate (Supplementary Figure 9D; n = 8 mice).

We repeated OFL using the standard protocol to compare animals with and without microglial ablation in the right mPFC (Figure 5F). Freezing levels on both day 2 and day 3 were comparable between groups, consistent with a ceiling effect under these conditions (Figure 5G, H, Supplementary Figure 9E–G; Vehicle, n = 7 mice; Clodronate, n = 7 mice). We then assessed thermal sensitivity using the TPP test (30 °C vs. 40 °C) and found that vehicle-injected mice did not differ from naïve controls ("No task"), indicating that OFL alone did not alter thermal nociception (Figure 5I). In contrast, mice that underwent OFL in the absence of microglia (clodronate-injected) showed significantly increased thermal aversion (Figure 5I). This effect was absent in clodronate-injected mice exposed to the task chamber without a demonstrator (Figure 5G–I, Supplementary Figure 9F, G; Clodronate Dem (−), n = 7 mice). To confirm the involvement of plasticity-related signaling in thermal sensitivity, we unilaterally inhibited CaMKII signaling by injecting AIP and subsequently ablated microglia on the same side (Supplementary Figure 10A–C). AIP expression occluded the clodronate-induced enhancement of thermal sensitivity after OFL under the standard protocol (Supplementary Figure 10D–J; AIP and Vehicle, n = 6 mice; AIP and Clodronate, n = 6 mice). These results support that the microglial ablation enhances thermal sensitivity through plasticity-dependent mechanisms.

Together, these findings demonstrate that, in the absence of microglia, social fear learning can aberrantly amplify pain sensitivity, leading to experience-dependent cross-talk between emotional circuits and highlighting a functional role for mature microglia in stabilizing established circuits during learning.

In contrast to the rapid remodeling of the mPFC network during social learning (69), fear learning based on direct experience induces slower remodeling of the mPFC (115), suggesting a lower demand on rapid plasticity. To confirm this, we performed auditory fear conditioning using direct fear experience. Mice received four tone–shock pairings on day 1 (Supplementary Figure 8D), followed by tone presentations on day 2. Unlike its effect on OFL, CaMKII inhibition through AIP expression in the mPFC did not impair the rapid acquisition of fear conditioning from direct experience (Supplementary Figure 8E, F; mCherry, n = 6 mice; AIP, n = 5 mice), consistent with previous evidence of delayed synaptic remodeling in the mPFC (115). Similarly, microglial ablation in the right mPFC did not affect conditioning or subsequent thermal sensitivity (Figure 5J, K, Supplementary Figure 9H, I; Vehicle, n = 7 mice; Clodronate, n = 8 mice). These findings highlight a selective requirement for finely tuned plasticity mechanisms to support rapid social learning without inducing emotional cross-talk.

Discussion

We found that microglia play a key role in the developmental shift of plasticity rules from a Hebbian plasticity form to a three-factor plasticity form in the mPFC during the transition from juvenile to adolescent stages. After maturation, microglia acquire the ability to suppress Hebbian plasticity through a humoral factor, and this suppression is counteracted by β_2-adrenergic

receptor–mediated cAMP signaling, enabling sLTP and rapid social learning. Based on these findings, we propose a microglia-mediated three-factor rule in which microglia gate synaptic potentiation by requiring noradrenergic input as a third factor. Moreover, this microglia-mediated suppression of Hebbian plasticity prevents social fear learning from spilling over into heightened pain sensitivity, suggesting that microglia tune the balance between plasticity and rigidity to preserve emotional circuit specificity in the mature mPFC.

We isolated the postsynaptic component of a neocortical Hebbian plasticity rule at single spine level using two-photon glutamate uncaging during the transition from juvenile to adolescent stages. We confirmed its developmental decline of sLTP across this period, consistent with previous reports (14, 19–22). In contrast to earlier models attributing this decline to neuron-intrinsic mechanisms (18–20, 116, 117), our results show that microglia play a critical role, likely through the humoral release of TNF-α, while pyramidal neurons retain their plastic potential at least until 7 weeks of age (Figure 1H). Although we cannot fully exclude the possibility that microglial suppression of sLTP reflects artefacts related to slice preparation, behavioral experiments involving β_2-AR inhibition and microglial ablation support the microglial suppression model. Unlike inhibitory mechanisms that irreversibly constrain plasticity after the critical period closure (118), microglial suppression is unique in that it can be rapidly reversed by a single physiological signal of NA.

In the adolescent mPFC, a three-factor rule for sLTP induction is achieved through NA, which counteracts microglia-dependent suppression, extending prior findings on the role of NA/β-AR/cAMP/PKA signaling in promoting neocortical LTP (13, 27, 97, 119–121). Consistent

403 with earlier studies showing that neuronal cAMP/PKA signaling is essential for LTP (122) and
404 sLTP (71, 123), we found that NA-dependent neocortical sLTP required PKA activity in
405 pyramidal neurons, as evidenced by the blockade of sLTP when the PKA inhibitor PKI was
406 included in the recording pipette (Figure 3G). Since neuronal PKA is canonically driven by
407 synaptic activity and calcium influx (124), these results support a dual-regulation model: while
408 neuronal PKA drives the intracellular signaling for sLTP induction, this machinery is
409 constitutively clamped by a microglial brake; Consequently, neuronal PKA activation alone was
410 insufficient to induce sLTP in the mature mPFC; β_2-ARs/cAMP signaling in microglia was
411 additionally required to relieve this suppression. In contrast to the facilitatory role of microglial
412 β_2-ARs in governing the three-factor rule for sLTP induction, a previous *in vivo* study in the
413 visual cortex reported a suppressive role for microglial β_2-ARs in spine remodeling through
414 regulation of microglial surveillance over the course of days (52). These findings suggest that
415 microglial β_2-ARs may operate on two distinct timescales to control spine remodeling in
416 opposing directions.

417 A critical question concerns the timescale of NA and TNF-α dependent modulation. Given that
418 TNF-α mediates plasticity suppression, NA may act by reducing TNF-α release, consistent with
419 its known immunomodulatory effects in monocytes (125, 126) and macrophages (127, 128).
420 Alternatively, NA may trigger the release of a neutralizing factor that counteracts TNF-α. In
421 either case, it is crucial whether the suppression of TNF-α can explain the rapid recovery of sLTP
422 observed within minutes of NA application. Although real-time monitoring of endogenous
423 TNF-α or downstream dynamics at the synapse level remains technically challenging, several
424 lines of evidence support the physiological plausibility of this rapid switching. First,

425 GPCR-mediated cAMP signaling is generally immediate, occurring within seconds (129).
426 Second, the synaptic actions of TNF-α are known to be highly dynamic; previous studies have
427 established that TNF-α can regulate AMPA receptor trafficking and synaptic efficacy within 10
428 minutes (91, 130). This suggests that the brake imposed by TNF-α is not a static structural
429 constraint but a continuously active signaling pressure that, once removed, allows the synaptic
430 machinery to engage quickly. Thus, despite the methodological difficulty in directly visualizing
431 the rapid dynamics of extracellular TNF-α, the rapid relief of microglial suppression provides a
432 plausible explanation for the gating of plasticity rules.

433 The NA, β_2-ARs, and CaMKII-dependent signaling for the three-factor rule appears to contribute
434 to the rapid establishment of social learning in the mPFC. Our data supports that the mPFC
435 undergoes active synaptic remodeling during observational learning (69), rather than merely
436 relaying social information. In contrast, this pathway was dispensable for learning from direct
437 experience, consistent with prior reports showing that mPFC synaptic potentiation emerges only
438 days after direct conditioning (115). NA levels rise in the mPFC during both observation and
439 direct shock (Figure 4E, Supplementary Figure 7H), indicating that NA release alone does not
440 account for the selective engagement of plasticity during social learning. Instead, we propose
441 that distinct patterns of glutamatergic activity during social observation uniquely recruit mPFC
442 plasticity. Supporting this idea, microglial ablation enhanced pain sensitivity only after social,
443 but not direct, fear learning (Figure 5I, K). Crucially, this phenotype appeared without altering
444 baseline pain thresholds or freezing behavior during acquisition, ruling out systemic
445 hypersensitivity. Furthermore, this behavior was plasticity-dependent as inhibiting CaMKII with
446 AIP during learning occluded the effect of microglial ablation (Supplementary Figure 10). This

447 supports that the aberrant behavior involves unconstrained synaptic plasticity, rather than the loss
448 of other microglial functions such as homeostatic support per se. Given that mPFC neurons often
449 exhibit mixed selectivity (131), including overlapping representations of vicarious fear and
450 pain-related signals (68), plasticity must be tightly constrained, as uncontrolled synaptic changes
451 can destabilize mature networks (30, 31). By ablating microglia, we directly demonstrated that
452 microglial gating restricts experience-driven modifications to prevent aberrant circuit cross-talk
453 in the mature mPFC. Thus, the three-factor rule mediated by NA–microglia interactions may
454 gate synaptic modifications within an optimal range, contributing to the functional integrity of
455 emotional circuits.

456 A similar NA–microglia-dependent plasticity rule shifting may operate in other neocortical
457 regions. Rapid spine remodeling has been observed in motor and sensory cortices *in vivo*
458 *(38–40)*, where sLTP is limited by glutamatergic stimulation alone in the visual cortex (44, 132),
459 but not in the motor cortex (133), suggesting plasticity rule shifting in select neocortical regions
460 including the mPFC and visual cortex. After maturation, three-factor rules may operate on
461 different timescales across neocortical regions, as NA signaling during social fear learning is
462 sustained over minutes in the mPFC (Figure 4E), whereas visual cortical synapses respond to NA
463 within seconds to modulate plasticity (29, 119). Future study may clarify how the
464 NA–microglia-dependent mechanism contributes to neocortical plasticity algorithms across
465 regions and developmental stages. Notably, whereas microglia suppressed plasticity and learning
466 in the mPFC, microglia in the hippocampus facilitate fear conditioning driven by direct

experience (55, 134), underscoring region-specific roles of microglia in plasticity and learning rules.

In conclusion, microglia play a central role in regulating developmental transitions in synaptic plasticity rules within the mPFC. Incorporating such developmental shifts in learning rules into computational models of learning may provide new insights into how neural circuits balance plasticity and rigidity (31). Future studies will reveal molecular mechanisms in microglia controlling this transition. The transition from juvenile to adolescent stages represents a critical window for the emergence of psychiatric disorders (135), during which microglia have been increasingly implicated in disease pathophysiology (136). Elucidating roles of microglia-dependent developmental shifts in plasticity rules in pathological contexts may therefore provide a cellular framework for understanding psychiatric vulnerability.

Acknowledgement

We thank Y. Li for the GRAB sensor plasmid; K. Hagihara, R. Hira, H. Kasai, A. Kumar, T. Masuda, J. Nagai, T. Okuyama, K. F. Tanaka, and A. Uematsu for helpful discussions; and M. Asaumi, A. Abe, A. Kurabayashi, R. Miyashita, and A. Nishikawa for technical assistance. This work was supported by Brain/MINDS (19dm0207069 to S.Y.) and Multidisciplinary Frontier Brain and Neuroscience Discoveries (Brain/MINDS 2.0) (JP23wm0625001, JP24wm0625308, JP24wm0625101 to S.Y.) from AMED; Grants-in-Aid (JP21H05171, JP21H05176, and 24K02115 to S.Y.) from JSPS; Moonshot R&D (JPMJMS2021 to S.Y.) from JST; The Uehara Memorial Foundation (to S.Y.); and The Mitsubishi Foundation (to S.Y.).

Author contribution

S.Y. conceptualized the study. M.T. performed and A.I. and Y.I. assisted slice experiments. H.O. performed and T.S. assisted behavioral experiments. H.E. produced AAV vectors. All the authors interpreted the data. S.Y., M.T and H.O. drafted and all the authors edited the manuscript.

Declaration of interests

The authors declare no competing interests.

Data availability

All data needed to evaluate the conclusions in the paper are present in the paper.

495 # Methods

496 *Animals*

497 C57BL/6J mice were purchased from Sankyo lab service. Tmem119-CreERT2 mice
498 [C57BL/6-Tmem119 (Cre/ERT2) Gfng/J; stock #031820] (70), Ai14 mice [B6.Cg-Gt (ROSA)
499 26Sortm14 (CAG-tdTomato) Hze/J; stock #007914] and R26-LSL-hM4Di-mCitrine mice
500 [B6.129-Gt (ROSA) 26Sortm1 (CAG-CHRM4*,-mCitrine) Ute/J; stock #026219] (105) were
501 obtained from the Jackson Laboratory. Mice were housed on a 12-hour/12-hour light/dark cycle
502 with *ad libitum* access to food and water. All animal experiments were approved by the Animal
503 Experimental Committee of the Faculty of Medicine at the University of Tokyo.

504 *Plasmids and adeno-associated viruses (AAV)*

505 For AAV production, we prepared the following constructs using PCR and Infusion (Takara):
506 pAAV-CaMKII(0.3)-FAS-NLS-mCherry-W and
507 pAAV-CaMKII(0.3)-FAS-NLS-mCherry-P2A-AIP-W, where FAS is loxP-FAS that has no effect
508 in this study, NLS is nuclear localisation sequence, AIP autocamtide 2-related inhibitory peptide
509 (KKALRRQEAVDAL), and P2A a self-cleaving peptide or obtained a plasmid from Addgene
510 (pAAV-hSyn-GRAB-NE2m-W, #208686) (112). AAVs were produced and their titres were
511 measured as described previously (137). Briefly, AAV expression vector, pHelper (Stratagene)
512 and either pRepCap AAV5 (Applied Viromics) or pUCmini-iCAP-PHP.eB (#103005, Addgene)
513 were transfected into HEK293 cells (AAV293, Stratagene). After three days, cells were harvested

514 and AAV were purified twice using ultracentrifuge with iodixanol. The titres for AAV (genome
515 copies, GC) were estimated using quantitative PCR.

516 *Surgery*

517 For AAV injection, mice were anesthetized with isoflurane (1-3%) and placed in a stereotaxic
518 frame (Narishige). AAVs were bilaterally (AIP experiments) or unilaterally (photometry
519 experiments) infused into the mPFC (AP +1.8 mm, ML ±0.3 mm, DV +2.4 mm for slice
520 experiments; AP +1.1 mm, ML ±0.3 mm, DV +2.0 mm for behavioral experiments) and using a
521 glass needle at a rate of 100 nl/min. Either of following AAVs was infused 1 μl per hemisphere:

522 - AAV2/5: CaMKII(0.3)-FAS-NLS-mCherry-W (2.0×10^{13} GC/ml)

523 - AAV2/5: CaMKII(0.3)-FAS-NLS-mCherry-P2A-AIP-W (2.0×10^{13} GC/ml)

524 - AAV2/PHP.eB: hSyn-GRAB-NE_{2m}-W (2.0×10^{13} GC/ml)

525 The glass needle was withdrawn 5 minutes after the end of the infusion. For photometry
526 experiments, the optical cannula (NA 0.5, 200 μm in diameter, 3.0 mm in length, RWD) was
527 placed in the same coordinate to the injection. The mice were allowed to recover in their home
528 cages for at least 2 weeks before slice or behavioral experiments.

529 For slice experiments with microglia ablation (53), 1 μl of 7 mg/ml clodronate (HY-B0657A,
530 MCE) or clophosome (F70101C-N, Funakoshi) was injected following the same protocol used
531 for virus injections. As vehicle controls, either ACSF or liposome (F70101-N, Funakoshi) was

532 used. Since no significant difference was observed between the effects of clodronate and
533 clophosome, the results were pooled for analysis.

534 For behavioral experiments with microglia ablation, 0.5 µl of 3 mg/ml clodronate was injected
535 into the right mPFC (AP +1.1 mm, ML +0.3 mm, DV +2.0 mm).

536 For drug cannula placement for behavioral experiments, a double cannula (26-gauge, Plastic One
537 or RWD) was placed to target the bilateral mPFC (AP +1.1 mm, ML ±0.3 mm, DV +2.0 mm).

538 *Acute slice preparation*

539 Acute coronal slices (280 µm thick) containing the mPFC were obtained from 2- to 7- week-old
540 female and male mice. Mice were anesthetized using isoflurane and then perfused transcardially
541 by ice-cold solution (220 mM sucrose, 3 mM KCl, 8 mM $MgCl_2$, 1.25 mM NaH_2PO_4, 26 mM
542 $NaHCO_3$, and 25 mM glucose) and were quickly decapitated. Brains were removed and sliced
543 with a microtome (VT1200, Leica). The slices were incubated at 34°C for 30 minutes and then at
544 room temperature in ACSF (125 mM NaCl, 2.5 mM KCl, 1 mM $CaCl_2$, 2 mM $MgCl_2$, 1.25 mM
545 NaH_2PO_4, 26 mM $NaHCO_3$, 20 mM glucose, and 200 µM Trolox (238813, Merck) which was
546 bubbled with 95% O_2 and 5% CO_2. Then, the slices were transferred to a recording chamber and
547 perfused with the ACSF solution described above, except using 2 mM $CaCl_2$ and 1 mM $MgCl_2$,
548 or 2 mM $CaCl_2$ and 0 mM $MgCl_2$ for magnesium-free experiments. All physiological
549 experiments were performed at 30–32 °C.

Structural plasticity in slices

Two-photon imaging of dendritic spines was performed using an upright microscope (BX61WI, Olympus) equipped with an FV1200 laser-scanning system (Olympus) with GaAsP photomultiplier tubes (Hamamatsu Photonics) and a water-immersion objective lens (NA 1.0, LUMPlanFI/IR, ×60, Olympus). The system included two mode-locked, femtosecond-pulse Ti:sapphire lasers (MaiTai, Spectra Physics). One was set at a wavelength of 720 nm for the uncaging of glutamate and the other was set at 980 nm for imaging. Fluorescence intensities of green and red fluorophores were detected through 500−550 nm (F03-525/50, Semrock) and 600−680 nm (ET642/80m, Chroma) filters, respectively after a dichroic mirror (T585lpxr, Chroma).

For whole-cell recordings, the patch pipettes (5−8 MΩ) were filled with a solution containing 120 mM potassium gluconate, 20 mM KCl, 10 mM disodium phosphocreatine, 4 mM ATP (magnesium salt), 0.3 mM GTP (sodium salt), 10 mM HEPES, 50 μM Alexa 488 hydrazide (A10436, Thermo Fisher Scientific) or Alexa 594 hydrazide (A10438, Thermo Fisher Scientific) and 5 μM β-actin (APHL99, Cytoskeleton), whose pH and osmolarity were adjusted to 7.25 and 275−280 mOsm by KOH and sucrose, respectively. We did not include Ca^{2+} buffer in the internal solution. For pharmacological experiments, protein kinase A inhibitor (10 μM, 6211, Tocris) was included in the pipette. The cells were voltage-clamped at −70 mV except during stimulation. Cells were discarded if spontaneous action potentials were observed during the stimulating period.

570 CDNI-glutamate (4 mM, Nard Institute) was locally puffed from a pipette. In experiments with
571 L-noradrenaline hydrochloride (50 μM, #74480, Merck), dopamine hydrochloride (50 μM,
572 D5662, Fujifilm) and clenbuterol (10 μM, C2691, TCI), the reagents were also included in the
573 puff pipette solution. For glutamate uncaging, a 720-nm laser was set to 4−6 mW, depending on
574 the depth to compensate for the decline in stimulation efficiency. Excitatory postsynaptic
575 currents (EPSCs) were recorded by stimulating 3 to 4 spines for 0.6 ms for each while cells were
576 clamped at -70 mV. After confirming the successful induction of EPSCs, structural plasticity was
577 induced by a spike-timing-dependent plasticity (STDP) protocol as previously described (71,
578 72). Briefly, one burst was composed of three back-propagating action potentials (bAPs, at 100
579 Hz) preceded by a single EPSP ($\Delta t = +10$ ms) induced by two-photon uncaging of
580 CDNI-glutamate. One train of STDP consisted of ten bursts repeated at 10 Hz. Fifteen trains of
581 stimulation were repeated at 0.1 Hz. APs were induced by injection of a depolarizing current of
582 1.5−2.0 nA for 2 ms. Dendrites containing spines within 100 μm of the soma and 20−50 μm in
583 depth were subjected to plasticity induction. For each experiment, three to four spines were
584 stimulated.

585 In experiments with D-AP5 (50 μM, #0106, Tocris Bioscience), ICI118,551 (1 μM, ab120808,
586 Abcam), metoprolol (1 μM, M5391, Merck), cilostamide (1 μM, S5806, Selleck), rolipram (1
587 μM, #180-01411, Fujifilm), deschloroclozapine (DCZ, 100 nM, #7193, Tocris)(*78–80*), TAPI-0
588 (1 μM, 579050, Calbiochem), pomalidomide (100 μM, P2074, TCI), mouse recombinant tumor
589 necrosis factor-α (TNF-α, 10 nM, 207-13463, Fujifilm), or mouse recombinant interleukin-1β

590 (IL-1β, 1 ng/ml, 094-04681, Fujifilm), slices were constantly perfused with the reagent
591 throughout the series of imaging.

592 In acute slices following clodronate injection, regions lacking microglia were identified by the
593 absence of fluorescence in transgenic mice expressing tdTomato in microglia. In some
594 experiments, clodronate or vehicle was injected into wild-type mice. Even in these wild-type
595 mice, the ablation site was reliably identified by a needle trace, and cells were recorded within
596 200 μm of the trace. The site was later confirmed histologically through immunostaining.

597 *Observational fear learning*

598 Before performing observational fear learning, mice were co-caged for 4 days in their home
599 cage. On day 1, an observer mouse was placed in a conditioning chamber with a stainless-steel
600 rod floor (30 cm × 30 cm, Melquest) for 5 minutes, during which two uncued footshocks (0.4
601 mA, 2 s each, 1-minute interval; shock generator, No. SG1000-S, Melquest) were delivered. The
602 mice were then returned to their home cage.

603 On day 2, the mice were placed in a different chamber (17 cm × 35 cm, Melquest), which was
604 divided into two sections: one with a plastic floor for the observer mouse, and the other with a
605 metal rod floor for a naive cagemate (the demonstrator). After 5 minutes of habituation, the
606 demonstrator mouse received 24 successive cued footshocks (tone: 6 kHz, 80−85 dB, 5 s;
607 footshock: 0.7 mA, 2 s, 10-second interval). The observer mouse was then returned to its home
608 cage with its cagemate.

609 On day 3, memory was assessed by placing the observer mice back into the observation chamber
610 in the same context and presenting three cues (6 kHz tone; 80−85 dB; 60 s; with intervals of 165
611 s and 177 s). For subthreshold conditioning, 12 cued weak foot shocks (0.2 mA, 2 s each) were
612 presented to the observer mice on day 2.

613 The stimulus presentation was controlled by triggers generated through a DAQ board
614 (PCIe-6223, National Instruments) using custom-written software. The entire session was
615 recorded with a camera (CS235MU, Thorlab) at 20 fps, synchronized with the stimulus
616 presentation through the DAQ board.

617 For experiments involving drug infusion, the double cannula was connected to a syringe
618 (1801RN, Hamilton) via a tube containing either the β_2 blocker ICI118,551 (200 μM in ACSF) or
619 ACSF alone, while the mice were under anesthesia (1% isoflurane, Fujifilm). The drug was
620 infused at a rate of 0.1 μl/min, with a total volume of 1 μl, controlled by a microsyringe pump
621 (Legato 111, KD Scientific). Mice were allowed to recover for at least 30 minutes before
622 undergoing conditioning.

623 For experiments involving clodronate, mice were euthanized a few days after the memory test,
624 and the patterns of ablation were assessed by immunohistochemistry.

625 *Auditory conditioning with direct fear experience*

626 On day 1, mice were placed in the conditioning chamber (metal rod floor and plexiglass
627 chamber, stripe wall) for 3 minutes and subsequently received pairs of cues (6kHz tone, 20 s)
628 and footshocks (0.7 mA, 1 s at the offset of tone) for 4 times with 60−79 s pseudo-randomized

intervals. On day 2, mice were placed in another context (dot wall) and the cues were presented 4 times with 60−77 s pseudo-randomized intervals. The entire session was recorded with a camera (CS235MU, Thorlab) at 20 fps.

Thermal place preference test

Thermal preference behavior was assessed using a two-zone apparatus consisting of two adjoining aluminum plates (100 mm × 100 mm each), whose temperatures were independently controlled. The plates formed a continuous flat floor joined by a copper bridge and enclosed by clear acrylic walls (400 mm high), creating a test arena measuring 220 mm × 100 mm. Mice were recorded at 20 frames per second using a side-mounted video camera.

Prior to testing, mice were habituated to the behavioral room for 10 minutes. Each mouse was then placed into the apparatus, with one plate set to a neutral 30 °C and the other to 40 °C. The side assignment of the warmer plate was counterbalanced across animals. Mice were recorded for 10 minutes, and the final 5 minutes were used to calculate place preference (66). Mice that urinated during the session were excluded from analysis.

Fiber photometry

A 470 nm LED (M470F3, Thorlabs) and 405nm LED (M405F1, Thorlabs) were pulsed (2 ms at 20 Hz, 10 to 15 μW) with shifting 20 ms in order to separate the excitation timing. The excitation light was passed through an excitation filter (ET405/20x; PCR47030x, Chroma Technology), dichroic mirrors (DMLP425, Thorlab; ZT488rdc, Chroma Technology), an objective lens (Olympus, UPlanFLN 20x), then through a rotary joint (RJ-1, Thorlabs) and finally into a

649 low-autofluorescence patch cord (custom made, Thorlabs) connected to the optical implant in the
650 mouse. Emission light was collected through the same patch cord, then passed back through the
651 cube with the dichroic mirror and a fluorescence filter (ET525/50m, Chroma Technology), and
652 then detected by a GaAsP detector (PMT2101/M, Thorlabs). Voltages from the photomultiplier
653 were bandpass filtered (1k Hz) and collected through the DAQ board used for the behavioral
654 experiments.

655 *Drug administration*

656 For adolescent mice, Tamoxifen (HY-13757A, MedChemExpress, 100 mg/kg body weight)
657 dissolved in corn oil was administered via intraperitoneal injection five times, with 48-hour
658 intervals between doses. Mice were monitored for at least one week before the experiments
659 commenced. For juvenile mice, 20 μg of tamoxifen dissolved in sunflower oil was administered
660 via intragastric injection at P3-5.

661 *Histology*

662 Mice were anesthetized with isoflurane, perfused using 4% paraformaldehyde (PFA), and
663 decapitated. Brains were post-fixed by 4% PFA overnight and then coronally sectioned at 50 μm
664 using a vibratome (VT-1000, Leica). For immunostaining, slices were incubated in PBS-T (0.2%
665 triton-X in PBS) containing 5% normal goat serum (NGS) at room temperature for 1 h. Slices
666 were then incubated with primary antibodies of rabbit anti-Iba1 antibody (1:1000, #019-19741,
667 Fujifilm) in PBS-T containing 5% NGS for 48 h at 4°C. After washing with PBS-T, slices were
668 incubated with secondary antibodies conjugated with Alexa 488 or Alexa 594 (goat anti-rabbit

669 IgG antibody, 1:500, A-11008 or A-11012, Thermo Fisher Scientific) for 2 h at room
670 temperature. For nuclear staining, TO-PRO-3 (1:2000, T3605, Thermo Fisher Scientific) was
671 incubated simultaneously with the secondary antibodies. The slices were mounted in antifade
672 reagents (H-1000, Vectashield, Vector Laboratories). The slices were subjected to imaging by
673 confocal microscopy (TCS−SP5, Leica) or fluorescent microscopy with structured illumination
674 (BZX-810, Keyence).

675 Contours were traced by referring to the Allen Mouse Brain Atlas
676 (https://mouse.brain-map.org/static/atlas).

677 *Data analysis*

678 For spine volume analysis, three-dimensional reconstructions of dendritic morphology were
679 generated by the summation of z-stacked images separated by 0.5 μm. The fluorescence intensity
680 of dendritic spines was normalized by the entire fluorescence of an imaging area. Spine-head
681 volumes were estimated from the total fluorescence intensity. Neighboring spines were defined
682 as spines within 3 μm of the stimulated spines. The baseline value for spine volume was
683 calculated as the mean of the spine volumes at 3 time points before uncaging. To calculate
684 volume change, the baseline was subtracted from the spine volume at each time point. Averaged
685 volume changes at 40 and 50 minutes after STDP stimulation were calculated and were further
686 averaged over spines in the same dendrite for statistical analyses.

687 For microglia contact analysis, microglial morphology was assessed by summing z-stacked
688 images taken at 1 μm intervals across 5 slices, centered on the plane of maximal intensity for

689 each dendritic spine. At each time point, the presence of microglial processes was recorded if the
690 average signal within a region of interest (ROI) with a 4 μm diameter around the stimulated
691 spine exceeded 3 standard deviations above the background signal of a nearby area.

692 For image analysis in behavioral experiments assessing the spread of AIP expression or
693 microglial ablation, z-stacked images were processed with a Gaussian filter, and
694 autofluorescence signals from the neocortex were subtracted. Images from all mice were
695 subsequently registered and averaged. For the analysis of AIP expression, the images were
696 binarized prior to averaging. In the AIP experiment for observational fear learning, two mice
697 exhibiting no AIP expression and two mice with the center of AIP expression deviating 0.6 mm
698 anterior to the target were excluded from the analyses. No mice were excluded in the microglial
699 ablation experiment.

700 For freezing analysis from behavioral data, mouse morphology was detected in each video frame
701 using custom-written scripts with OpenCV in Python. Frame-by-frame differences were then
702 calculated and thresholded to identify freezing responses.

703 For photometry data, signals from 470 nm and 405 nm excitation were subtracted from
704 autofluorescent reference values. The signal was median-filtered and down-sampled to 2 Hz.
705 Ratio of signal was calculated for each session.

706 For thermal preference analysis from behavioral data, mouse location was annotated in each
707 video frame using napari in Python. Frame ratios for occupying the lower temperature chamber
708 were then calculated.

Statistical tests

We used the Kruskal–Wallis test with post hoc Steel's test or Wilcoxon signed-rank test with Bonferroni correction after Friedman test for multiple comparisons, the Mann–Whitney U test, or the Wilcoxon signed-rank test, depending on the experimental design. Results were considered significant if $P < 0.05$ in two-sided tests. Sample sizes were determined based on previous experiments (71, 72).

References

1. D. V. Buonomano, M. M. Merzenich, Cortical plasticity: from synapses to maps. *Annu Rev Neurosci* **21**, 149–186 (1998).
2. D. E. Feldman, Synaptic Mechanisms for Plasticity in Neocortex. *Annu. Rev. Neurosci.* **32**, 33–55 (2009).
3. Hebb, D. O., The organization of behavior: A neuropsychological theory. *Sci. Educ.*, doi: 10.1002/sce.37303405110 (1949).
4. H. Markram, J. Lübke, M. Frotscher, B. Sakmann, Regulation of synaptic efficacy by coincidence of postsynaptic APs and EPSPs. *Science* **275**, 213–215 (1997).
5. M. F. Bear, Bidirectional synaptic plasticity: from theory to reality. *Philos. Trans. R. Soc. Lond. Ser. B: Biol. Sci.* **358**, 649–655 (2003).
6. Y. Dan, M.-M. Poo, Spike timing-dependent plasticity of neural circuits. *Neuron* **44**, 23–30 (2004).
7. N. Frémaux, W. Gerstner, Neuromodulated Spike-Timing-Dependent Plasticity, and Theory of Three-Factor Learning Rules. *Front. Neural Circuits* **9**, 85 (2016).
8. Ł. Kuśmierz, T. Isomura, T. Toyoizumi, Learning with three factors: modulating Hebbian plasticity with errors. *Curr Opin Neurobiol* **46**, 170–177 (2017).
9. W. Gerstner, M. Lehmann, V. Liakoni, D. Corneil, J. Brea, Eligibility Traces and Plasticity on Behavioral Time Scales: Experimental Support of NeoHebbian Three-Factor Learning Rules. *Front Neural Circuits* **12**, 53 (2018).
10. A. Kirkwood, M. G. Rioult, M. F. Bear, Experience-dependent modification of synaptic plasticity in visual cortex. *Nature* **381**, 526–528 (1996).
11. J. Grutzendler, N. Kasthuri, W.-B. Gan, Long-term dendritic spine stability in the adult cortex. *Nature* **420**, 812–816 (2002).
12. V. Wespatat, F. Tennigkeit, W. Singer, Phase Sensitivity of Synaptic Modifications in Oscillating Cells of Rat Visual Cortex. *J. Neurosci.* **24**, 9067–9075 (2004).
13. G. H. Seol, J. Ziburkus, S. Huang, L. Song, I. T. Kim, K. Takamiya, R. L. Huganir, H.-K. Lee, A. Kirkwood, Neuromodulators control the polarity of spike-timing-dependent synaptic plasticity. *Neuron* **55**, 919–929 (2007).
14. A. Kirkwood, H. K. Lee, M. F. Bear, Co-regulation of long-term potentiation and experience-dependent synaptic plasticity in visual cortex by age and experience. *Nature* **375**, 328–331 (1995).
15. V. Egger, D. Feldmeyer, B. Sakmann, Coincidence detection and changes of synaptic efficacy in spiny stellate neurons in rat barrel cortex. *Nat. Neurosci.* **2**, 1098–1105 (1999).
16. T. K. Hensch, Critical period plasticity in local cortical circuits. *Nat. Rev. Neurosci.* **6**, 877–888 (2005).
17. N. Caporale, Y. Dan, Spike Timing–Dependent Plasticity: A Hebbian Learning Rule. *Annu. Rev. Neurosci.* **31**, 25–46 (2008).

18. C. E. Yaeger, D. Vardalaki, Q. Zhang, T. L. D. Pham, N. J. Brown, N. Ji, M. T. Harnett, A dendritic mechanism for balancing synaptic flexibility and stability. *Cell Rep.* **43**, 114638 (2024).
19. Y. Edagawa, H. Saito, K. Abe, Endogenous serotonin contributes to a developmental decrease in long-term potentiation in the rat visual cortex. *J Neurosci* **21**, 1532–1537 (2001).
20. Y. Yoshimura, T. Ohmura, Y. Komatsu, Two forms of synaptic plasticity with distinct dependence on age, experience, and NMDA receptor subtype in rat visual cortex. *J Neurosci* **23**, 6557–6566 (2003).
21. T. J. Teyler, A. T. Perkins, K. M. Harris, The development of long-term potentiation in hippocampus and neocortex. *Neuropsychologia* **27**, 31–39 (1989).
22. B. Jiang, M. Treviño, A. Kirkwood, Sequential Development of Long-Term Potentiation and Depression in Different Layers of the Mouse Visual Cortex. *J. Neurosci.* **27**, 9648–9652 (2007).
23. G. M. Anlezark, T. J. Crow, A. P. Greenway, Impaired learning and decreased cortical norepinephrine after bilateral locus coeruleus lesions. *Science* **181**, 682–684 (1973).
24. J. D. Pettigrew, T. Kasamatsu, Local perfusion of noradrenaline maintains visual cortical plasticity. *Nature* **271**, 761–763 (1978).
25. M. F. Bear, W. Singer, Modulation of visual cortical plasticity by acetylcholine and noradrenaline. *Nature* **320**, 172–176 (1986).
26. D. Mueller, J. T. Porter, G. J. Quirk, Noradrenergic signaling in infralimbic cortex increases cell excitability and strengthens memory for fear extinction. *J Neurosci* **28**, 369–375 (2008).
27. H.-C. Zhou, Y.-Y. Sun, W. Cai, X.-T. He, F. Yi, B.-M. Li, X.-H. Zhang, Activation of β2-adrenoceptor enhances synaptic potentiation and behavioral memory via cAMP-PKA signaling in the medial prefrontal cortex of rats. *Learn Mem* **20**, 274–284 (2013).
28. A. R. O. Martins, R. C. Froemke, Coordinated forms of noradrenergic plasticity in the locus coeruleus and primary auditory cortex. *Nat Neurosci* **18**, 1483–1492 (2015).
29. S. Z. Hong, L. Mesik, C. D. Grossman, J. Y. Cohen, B. Lee, D. Severin, H.-K. Lee, J. W. Hell, A. Kirkwood, Norepinephrine potentiates and serotonin depresses visual cortical responses by transforming eligibility traces. *Nat Commun* **13**, 3202 (2022).
30. J. L. McClelland, B. L. McNaughton, R. C. O'Reilly, Why there are complementary learning systems in the hippocampus and neocortex: Insights from the successes and failures of connectionist models of learning and memory. *Psychol Rev* **102**, 419–457 (1995).
31. M. K. Benna, S. Fusi, Computational principles of synaptic memory consolidation. *Nat Neurosci* **19**, 1697–1706 (2016).
32. L. R. Squire, P. Alvarez, Retrograde amnesia and memory consolidation: a neurobiological perspective. *Curr. Opin. Neurobiol.* **5**, 169–177 (1995).
33. P. W. Frankland, B. Bontempi, The organization of recent and remote memories. *Nat. Rev. Neurosci.* **6**, 119–130 (2005).
34. M. Matsuzaki, N. Honkura, G. C. R. Ellis-Davies, H. Kasai, Structural basis of long-term potentiation in single dendritic spines. *Nature* **429**, 761–766 (2004).
35. H. Kasai, N. E. Ziv, H. Okazaki, S. Yagishita, T. Toyoizumi, Spine dynamics in the brain,

mental disorders and artificial neural networks. *Nat Rev Neurosci* **22**, 407–422 (2021).
36. J. Noguchi, A. Nagaoka, S. Watanabe, G. C. R. Ellis-Davies, K. Kitamura, M. Kano, M. Matsuzaki, H. Kasai, In vivo two-photon uncaging of glutamate revealing the structure-function relationships of dendritic spines in the neocortex of adult mice. *J Physiol (Lond)* **589**, 2447–2457 (2011).
37. S. Holler, G. Köstinger, K. A. C. Martin, G. F. P. Schuhknecht, K. J. Stratford, Structure and function of a neocortical synapse. *Nature* **591**, 111–116 (2021).
38. J. Cichon, W.-B. Gan, Branch-specific dendritic Ca(2+) spikes cause persistent synaptic plasticity. *Nature* **520**, 180–185 (2015).
39. S. El-Boustani, J. P. K. Ip, V. Breton-Provencher, G. W. Knott, H. Okuno, H. Bito, M. Sur, Locally coordinated synaptic plasticity of visual cortex neurons in vivo. *Science* **360**, 1349–1354 (2018).
40. W. J. Wright, N. G. Hedrick, T. Komiyama, Distinct synaptic plasticity rules operate across dendritic compartments in vivo during learning. *Science* **388**, 322–328 (2025).
41. C. D. Harvey, K. Svoboda, Locally dynamic synaptic learning rules in pyramidal neuron dendrites. *Nature* **450**, 1195–1200 (2007).
42. J.-I. Tanaka, Y. Horiike, M. Matsuzaki, T. Miyazaki, G. C. R. Ellis-Davies, H. Kasai, Protein synthesis and neurotrophin-dependent structural plasticity of single dendritic spines. *Science* **319**, 1683–1687 (2008).
43. H. Ucar, S. Watanabe, J. Noguchi, Y. Morimoto, Y. Iino, S. Yagishita, N. Takahashi, H. Kasai, Mechanical actions of dendritic-spine enlargement on presynaptic exocytosis. *Nature* **600**, 686–689 (2021).
44. J. Noguchi, A. Nagaoka, T. Hayama, H. Ucar, S. Yagishita, N. Takahashi, H. Kasai, Bidirectional in vivo structural dendritic spine plasticity revealed by two-photon glutamate uncaging in the mouse neocortex. *Sci Rep* **9**, 13922 (2019).
45. X. Yin, N. Jones, J. Yang, N. Asraoui, M.-E. Mathieu, L. Cai, S. X. Chen, Delayed motor learning in a 16p11.2 deletion mouse model of autism is rescued by locus coeruleus activation. *Nat Neurosci* **24**, 646–657 (2021).
46. R. S. Larsen, D. Rao, P. B. Manis, B. D. Philpot, STDP in the Developing Sensory Neocortex. *Front. Synaptic Neurosci.* **2**, 9 (2010).
47. C. N. Parkhurst, G. Yang, I. Ninan, J. N. Savas, J. R. Yates, J. J. Lafaille, B. L. Hempstead, D. R. Littman, W.-B. Gan, Microglia promote learning-dependent synapse formation through brain-derived neurotrophic factor. *Cell* **155**, 1596–1609 (2013).
48. F. Filipello, R. Morini, I. Corradini, V. Zerbi, A. Canzi, B. Michalski, M. Erreni, M. Markicevic, C. Starvaggi-Cucuzza, K. Otero, L. Piccio, F. Cignarella, F. Perrucci, M. Tamborini, M. Genua, L. Rajendran, E. Menna, S. Vetrano, M. Fahnestock, R. C. Paolicelli, M. Matteoli, The microglial innate immune receptor TREM2 is required for synapse elimination and normal brain connectivity. *Immunity* **48**, 979-991.e8 (2018).
49. A. Miyamoto, H. Wake, A. W. Ishikawa, K. Eto, K. Shibata, H. Murakoshi, S. Koizumi, A.

J. Moorhouse, Y. Yoshimura, J. Nabekura, Microglia contact induces synapse formation in developing somatosensory cortex. *Nat Commun* **7**, 12540 (2016).

50. R. Morini, E. Tagliatti, M. Bizzotto, M. Matteoli, Microglial and TREM2 dialogues in the developing brain. *Immunity* **58**, 1068–1084 (2025).

51. Y. U. Liu, Y. Ying, Y. Li, U. B. Eyo, T. Chen, J. Zheng, A. D. Umpierre, J. Zhu, D. B. Bosco, H. Dong, L.-J. Wu, Neuronal network activity controls microglial process surveillance in awake mice via norepinephrine signaling. *Nat Neurosci* **22**, 1771–1781 (2019).

52. R. D. Stowell, G. O. Sipe, R. P. Dawes, H. N. Batchelor, K. A. Lordy, B. S. Whitelaw, M. B. Stoessel, J. M. Bidlack, E. Brown, M. Sur, A. K. Majewska, Noradrenergic signaling in the wakeful state inhibits microglial surveillance and synaptic plasticity in the mouse visual cortex. *Nat Neurosci* **22**, 1782–1792 (2019).

53. K. Ji, G. Akgul, L. P. Wollmuth, S. E. Tsirka, Microglia actively regulate the number of functional synapses. *PLoS ONE* **8**, e56293 (2013).

54. L. Weinhard, G. di Bartolomei, G. Bolasco, P. Machado, N. L. Schieber, U. Neniskyte, M. Exiga, A. Vadisiute, A. Raggioli, A. Schertel, Y. Schwab, C. T. Gross, Microglia remodel synapses by presynaptic trogocytosis and spine head filopodia induction. *Nat Commun* **9**, 1228 (2018).

55. P. T. Nguyen, L. C. Dorman, S. Pan, I. D. Vainchtein, R. T. Han, H. Nakao-Inoue, S. E. Taloma, J. J. Barron, A. B. Molofsky, M. A. Kheirbek, A. V. Molofsky, Microglial remodeling of the extracellular matrix promotes synapse plasticity. *Cell* **182**, 388-403.e15 (2020).

56. M. E. Choudhury, K. Miyanishi, H. Takeda, A. Islam, N. Matsuoka, M. Kubo, S. Matsumoto, T. Kunieda, M. Nomoto, H. Yano, J. Tanaka, Phagocytic elimination of synapses by microglia during sleep. *Glia* **68**, 44–59 (2020).

57. Y.-J. Liu, E. Spangenberg, B. Tang, T. C. Holmes, K. N. Green, X. Xu, Microglia elimination increases neural circuit connectivity and activity in adult mouse cortex. *J Neurosci*, doi: 10.1523/jneurosci.2140-20.2020 (2020).

58. A. Uematsu, B. Z. Tan, E. A. Ycu, J. S. Cuevas, J. Koivumaa, F. Junyent, E. J. Kremer, I. B. Witten, K. Deisseroth, J. P. Johansen, Modular organization of the brainstem noradrenaline system coordinates opposing learning states. *Nat Neurosci* **20**, 1602–1611 (2017).

59. V. Breton-Provencher, G. T. Drummond, J. Feng, Y. Li, M. Sur, Spatiotemporal dynamics of noradrenaline during learned behaviour. *Nature* **606**, 732–738 (2022).

60. M. G. P. Feenstra, Dopamine and noradrenaline release in the prefrontal cortex in relation to unconditioned and conditioned stress and reward. *Prog. Brain Res.* **126**, 133–163 (2000).

61. A. Basu, J.-H. Yang, A. Yu, S. Glaeser-Khan, J. A. Rondeau, J. Feng, J. H. Krystal, Y. Li, A. P. Kaye, Frontal norepinephrine represents a threat prediction error under uncertainty. *Biol Psychiatry* **96**, 256–267 (2024).

62. J.-H. Kim, D.-E. Choi, H.-S. Shin, The lateralized LC-NAergic system distinguishes vicarious versus direct fear in mice. *Nat Commun* **16**, 2364 (2025).

63. S. M. Schalbetter, A. S. von Arx, N. Cruz-Ochoa, K. Dawson, A. Ivanov, F. S. Mueller,

H.-Y. Lin, R. Amport, W. Mildenberger, D. Mattei, D. Beule, C. Földy, M. Greter, T. Notter, U. Meyer, Adolescence is a sensitive period for prefrontal microglia to act on cognitive development. *Sci Adv* **8**, eabi6672 (2022).

64. D. Jeon, S. Kim, M. Chetana, D. Jo, H. E. Ruley, S.-Y. Lin, D. Rabah, J.-P. Kinet, H.-S. Shin, Observational fear learning involves affective pain system and Cav1.2 Ca2+ channels in ACC. *Nat Neurosci* **13**, 482–488 (2010).

65. S. A. Allsop, R. Wichmann, F. Mills, A. Burgos-Robles, C.-J. Chang, A. C. Felix-Ortiz, A. Vienne, A. Beyeler, E. M. Izadmehr, G. Glober, M. I. Cum, J. Stergiadou, K. K. Anandalingam, K. Farris, P. Namburi, C. A. Leppla, J. C. Weddington, E. H. Nieh, A. C. Smith, D. Ba, E. N. Brown, K. M. Tye, Corticoamygdala transfer of socially derived information gates observational learning. *Cell* **173**, 1329-1342.e18 (2018).

66. M. L. Smith, N. Asada, R. C. Malenka, Anterior cingulate inputs to nucleus accumbens control the social transfer of pain and analgesia. *Science* **371**, 153–159 (2021).

67. J. I. Terranova, J. Yokose, H. Osanai, S. K. Ogawa, T. Kitamura, Systems consolidation induces multiple memory engrams for a flexible recall strategy in observational fear memory in male mice. *Nat Commun* **14**, 3976 (2023).

68. J. Choi, Y.-B. Lee, D. So, J. Y. Kim, S. Choi, S. Kim, S. Keum, Cortical representations of affective pain shape empathic fear in male mice. *Nat Commun* **16**, 1937 (2025).

69. S. E. Silverstein, R. O'Sullivan, O. Bukalo, D. Pati, J. A. Schaffer, A. Limoges, L. Zsembik, T. Yoshida, J. J. O'Malley, R. F. Paletzki, A. G. Lieberman, M. Nonaka, K. Deisseroth, C. R. Gerfen, M. A. Penzo, T. L. Kash, A. Holmes, A distinct cortical code for socially learned threat. *Nature* **626**, 1066–1072 (2024).

70. T. Kaiser, G. Feng, Tmem119-EGFP and Tmem119-CreERT2 Transgenic Mice for Labeling and Manipulating Microglia. *eNeuro* **6** (2019).

71. S. Yagishita, A. Hayashi-Takagi, G. C. R. Ellis-Davies, H. Urakubo, S. Ishii, H. Kasai, A critical time window for dopamine actions on the structural plasticity of dendritic spines. *Science* **345**, 1616–1620 (2014).

72. Y. Iino, T. Sawada, K. Yamaguchi, M. Tajiri, S. Ishii, H. Kasai, S. Yagishita, Dopamine D2 receptors in discrimination learning and spine enlargement. *Nature* **579**, 555–560 (2020).

73. W.-N. Jin, S. X.-Y. Shi, Z. Li, M. Li, K. Wood, R. J. Gonzales, Q. Liu, Depletion of microglia exacerbates postischemic inflammation and brain injury. *J Cereb Blood Flow Metab* **37**, 2224–2236 (2017).

74. C. D. Harvey, R. Yasuda, H. Zhong, K. Svoboda, The Spread of Ras Activity Triggered by Activation of a Single Dendritic Spine. *Science* **321**, 136–140 (2008).

75. M. Bosch, J. Castro, T. Saneyoshi, H. Matsuno, M. Sur, Y. Hayashi, Structural and molecular remodeling of dendritic spine substructures during long-term potentiation. *Neuron* **82**, 444–459 (2014).

76. P. Berki, C. Cserép, Z. Környei, B. Pósfai, E. Szabadits, A. Domonkos, A. Kellermayer, M. Nyerges, X. Wei, I. Mody, A. Kunihiko, H. Beck, H. Kaikai, W. Ya, N. Lénárt, Z. Wu, M. Jing,

Y. Li, A. I. Gulyás, Á. Dénes, Microglia contribute to neuronal synchrony despite endogenous ATP-related phenotypic transformation in acute mouse brain slices. *Nat Commun* **15**, 5402 (2024).
77. M.-È. Tremblay, R. L. Lowery, A. K. Majewska, Microglial interactions with synapses are modulated by visual experience. *PLoS Biol* **8**, e1000527 (2010).
78. C. C. Escoubas, A. V. Molofsky, Microglia as integrators of brain-associated molecular patterns. *Trends Immunol* **45**, 358–370 (2024).
79. J. Cornell, S. Salinas, H.-Y. Huang, M. Zhou, Microglia regulation of synaptic plasticity and learning and memory. *Neural Regen Res* **17**, 705–716 (2022).
80. S. Ren, W. Yao, M. D. Tambini, T. Yin, K. A. Norris, L. D'Adamio, Microglia TREM2R47H Alzheimer-linked variant enhances excitatory transmission and reduces LTP via increased TNF-α levels. *eLife* **9** (2020).
81. K. Hoshino, K. Hasegawa, H. Kamiya, Y. Morimoto, Synapse-specific effects of IL-1β on long-term potentiation in the mouse hippocampus. *Biomed Res* **38**, 183–188 (2017).
82. J. T. Rogers, J. M. Morganti, A. D. Bachstetter, C. E. Hudson, M. M. Peters, B. A. Grimmig, E. J. Weeber, P. C. Bickford, C. Gemma, CX3CR1 deficiency leads to impairment of hippocampal cognitive function and synaptic plasticity. *J Neurosci* **31**, 16241–16250 (2011).
83. T. Liu, J. Lu, K. Lukasiewicz, B. Pan, Y. Zuo, Stress induces microglia-associated synaptic circuit alterations in the dorsomedial prefrontal cortex. *Neurobiol Stress*, 100342 (2021).
84. H. Wake, A. J. Moorhouse, S. Jinno, S. Kohsaka, J. Nabekura, Resting microglia directly monitor the functional state of synapses in vivo and determine the fate of ischemic terminals. *J Neurosci* **29**, 3974–3980 (2009).
85. S. E. Haynes, G. Hollopeter, G. Yang, D. Kurpius, M. E. Dailey, W.-B. Gan, D. Julius, The P2Y12 receptor regulates microglial activation by extracellular nucleotides. *Nat Neurosci* **9**, 1512–1519 (2006).
86. B. Tasic, Z. Yao, L. T. Graybuck, K. A. Smith, T. N. Nguyen, D. Bertagnolli, J. Goldy, E. Garren, M. N. Economo, S. Viswanathan, O. Penn, T. Bakken, V. Menon, J. Miller, O. Fong, K. E. Hirokawa, K. Lathia, C. Rimorin, M. Tieu, R. Larsen, T. Casper, E. Barkan, M. Kroll, S. Parry, N. V. Shapovalova, D. Hirschstein, J. Pendergraft, H. A. Sullivan, T. K. Kim, A. Szafer, N. Dee, P. Groblewski, I. Wickersham, A. Cetin, J. A. Harris, B. P. Levi, S. M. Sunkin, L. Madisen, T. L. Daigle, L. Looger, A. Bernard, J. Phillips, E. Lein, M. Hawrylycz, K. Svoboda, A. R. Jones, C. Koch, H. Zeng, Shared and distinct transcriptomic cell types across neocortical areas. *Nature* **563**, 72–78 (2018).
87. C. A. Davies, S. A. Loddick, S. Toulmond, R. P. Stroemer, J. Hunt, N. J. Rothwell, The progression and topographic distribution of interleukin-1beta expression after permanent middle cerebral artery occlusion in the rat. *J Cereb Blood Flow Metab* **19**, 87–98 (1999).
88. Y. Zhang, K. Chen, S. A. Sloan, M. L. Bennett, A. R. Scholze, S. O'Keeffe, H. P. Phatnani, P. Guarnieri, C. Caneda, N. Ruderisch, S. Deng, S. A. Liddelow, C. Zhang, R. Daneman, T. Maniatis, B. A. Barres, J. Q. Wu, An RNA-sequencing transcriptome and splicing database of

glia, neurons, and vascular cells of the cerebral cortex. *J Neurosci* **34**, 11929–11947 (2014).
89. M. R. P. Elmore, A. R. Najafi, M. A. Koike, N. N. Dagher, E. E. Spangenberg, R. A. Rice, M. Kitazawa, B. Matusow, H. Nguyen, B. L. West, K. N. Green, Colony-stimulating factor 1 receptor signaling is necessary for microglia viability, unmasking a microglia progenitor cell in the adult brain. *Neuron* **82**, 380–397 (2014).
90. X. Nie, S. Kitaoka, K. Tanaka, E. Segi-Nishida, Y. Imoto, A. Ogawa, F. Nakano, A. Tomohiro, K. Nakayama, M. Taniguchi, Y. Mimori-Kiyosue, A. Kakizuka, S. Narumiya, T. Furuyashiki, The Innate Immune Receptors TLR2/4 Mediate Repeated Social Defeat Stress-Induced Social Avoidance through Prefrontal Microglial Activation. *Neuron* **99**, 464-479.e7 (2018).
91. E. C. Beattie, D. Stellwagen, W. Morishita, J. C. Bresnahan, B. K. Ha, M. V. Zastrow, M. S. Beattie, R. C. Malenka, Control of synaptic strength by glial TNFalpha. *Science* **295**, 2282–2285 (2002).
92. N. Parameswaran, S. Patial, Tumor necrosis factor-α signaling in macrophages. *Crit Rev Eukaryot Gene Expr* **20**, 87–103 (2010).
93. F. Zunke, S. Rose-John, The shedding protease ADAM17: Physiology and pathophysiology. *Biochim Biophys Acta Mol Cell Res* **1864**, 2059–2070 (2017).
94. J.-Y. Wang, Y.-N. Huang, C.-C. Chiu, D. Tweedie, W. Luo, C. G. Pick, S.-Y. Chou, Y. Luo, B. J. Hoffer, N. H. Greig, J.-Y. Wang, Pomalidomide mitigates neuronal loss, neuroinflammation, and behavioral impairments induced by traumatic brain injury in rat. *J Neuroinflammation* **13**, 168 (2016).
95. J. Shortt, A. K. Hsu, R. W. Johnstone, Thalidomide-analogue biology: immunological, molecular and epigenetic targets in cancer therapy. *Oncogene* **32**, 4191–4202 (2013).
96. T. Masuda, R. Sankowski, O. Staszewski, C. Böttcher, L. Amann, Sagar, C. Scheiwe, S. Nessler, P. Kunz, G. van Loo, V. A. Coenen, P. C. Reinacher, A. Michel, U. Sure, R. Gold, D. Grün, J. Priller, C. Stadelmann, M. Prinz, Spatial and temporal heterogeneity of mouse and human microglia at single-cell resolution. *Nature* **566**, 388–392 (2019).
97. P. Sáez-Briones, R. Soto-Moyano, H. Burgos, A. Castillo, L. Valladares, C. Morgan, H. Pérez, R. Barra, L. Constandil, C. Laurido, A. Hernández, β2-adrenoceptor stimulation restores frontal cortex plasticity and improves visuospatial performance in hidden-prenatally-malnourished young-adult rats. *Neurobiol Learn Mem* **119**, 1–9 (2015).
98. L. Guo, H. Xiong, J.-I. Kim, Y.-W. Wu, R. R. Lalchandani, Y. Cui, Y. Shu, T. Xu, J. B. Ding, Dynamic rewiring of neural circuits in the motor cortex in mouse models of Parkinson's disease. *Nat Neurosci* **18**, 1299–1309 (2015).
99. H. Hu, E. Real, K. Takamiya, M.-G. Kang, J. Ledoux, R. L. Huganir, R. Malinow, Emotion enhances learning via norepinephrine regulation of AMPA-receptor trafficking. *Cell* **131**, 160–173 (2007).
100. D. G. Winder, K. C. Martin, I. A. Muzzio, D. Rohrer, A. Chruscinski, B. Kobilka, E. R. Kandel, ERK plays a regulatory role in induction of LTP by theta frequency stimulation and its

modulation by beta-adrenergic receptors. *Neuron* **24**, 715–726 (1999).
101. M. Murugan, H. J. Jang, M. Park, E. M. Miller, J. Cox, J. P. Taliaferro, N. F. Parker, V. Bhave, H. Hur, Y. Liang, A. R. Nectow, J. W. Pillow, I. B. Witten, Combined Social and Spatial Coding in a Descending Projection from the Prefrontal Cortex. *Cell* **171**, 1663-1677.e16 (2017).
102. L.-P. Bernier, C. J. Bohlen, E. M. York, H. B. Choi, A. Kamyabi, L. Dissing-Olesen, J. K. Hefendehl, H. Y. Collins, B. Stevens, B. A. Barres, B. A. MacVicar, Nanoscale Surveillance of the Brain by Microglia via cAMP-Regulated Filopodia. *Cell Rep* **27**, 2895-2908.e4 (2019).
103. C. G. Vecsey, G. S. Baillie, D. Jaganath, R. Havekes, A. Daniels, M. Wimmer, T. Huang, K. M. Brown, X.-Y. Li, G. Descalzi, S. S. Kim, T. Chen, Y.-Z. Shang, M. Zhuo, M. D. Houslay, T. Abel, Sleep deprivation impairs cAMP signalling in the hippocampus. *Nature* **461**, 1122–1125 (2009).
104. K. Yamaguchi, Y. Maeda, T. Sawada, Y. Iino, M. Tajiri, R. Nakazato, S. Ishii, H. Kasai, S. Yagishita, A behavioural correlate of the synaptic eligibility trace in the nucleus accumbens. *Sci Rep* **12**, 1921 (2022).
105. H. Zhu, D. K. Aryal, R. H. J. Olsen, D. J. Urban, A. Swearingen, S. Forbes, B. L. Roth, U. Hochgeschwender, Cre-dependent DREADD (Designer Receptors Exclusively Activated by Designer Drugs) mice. *Genesis* **54**, 439–446 (2016).
106. C. Ma, B. Li, D. Silverman, X. Ding, A. Li, C. Xiao, G. Huang, K. Worden, S. Muroy, W. Chen, Z. Xu, C. F. Tso, Y. Huang, Y. Zhang, Q. Luo, K. Saijo, Y. Dan, Microglia regulate sleep through calcium-dependent modulation of norepinephrine transmission. *Nat Neurosci* **27**, 249–258 (2024).
107. S. Zhao, L. Wang, D. Kleidonas, F. Qi, Y. Liang, J. Zheng, A. D. Umpierre, L.-J. Wu, Chemogenetic activation of microglial Gi signaling decreases microglial surveillance and impairs neuronal synchronization. *Sci. Adv.* **11**, eado7829 (2025).
108. Y. Nagai, N. Miyakawa, H. Takuwa, Y. Hori, K. Oyama, B. Ji, M. Takahashi, X.-P. Huang, S. T. Slocum, J. F. DiBerto, Y. Xiong, T. Urushihata, T. Hirabayashi, A. Fujimoto, K. Mimura, J. G. English, J. Liu, K.-I. Inoue, K. Kumata, C. Seki, M. Ono, M. Shimojo, M.-R. Zhang, Y. Tomita, J. Nakahara, T. Suhara, M. Takada, M. Higuchi, J. Jin, B. L. Roth, T. Minamimoto, Deschloroclozapine, a potent and selective chemogenetic actuator enables rapid neuronal and behavioral modulations in mice and monkeys. *Nat Neurosci* **23**, 1157–1167 (2020).
109. S. Yun, B. Yang, J. D. Anair, M. M. Martin, S. W. Fleps, A. Pamukcu, N.-H. Yeh, A. Contractor, A. Kennedy, J. G. Parker, Antipsychotic drug efficacy correlates with the modulation of D1 rather than D2 receptor-expressing striatal projection neurons. *Nat Neurosci* **26**, 1417–1428 (2023).
110. K. A. Han, T.-H. Yoon, J. Kim, J. Lee, J. Y. Lee, G. Jang, J. W. Um, J. K. Kim, J. Ko, Specification of neural circuit architecture shaped by context-dependent patterned LAR-RPTP microexons. *Nat Commun* **15**, 1624 (2024).
111. A. Olsson, E. Knapska, B. Lindström, The neural and computational systems of social learning. *Nat Rev Neurosci* **21**, 197–212 (2020).

1027 112. J. Feng, H. Dong, J. E. Lischinsky, J. Zhou, F. Deng, C. Zhuang, X. Miao, H. Wang, G. Li,
1028 R. Cai, H. Xie, G. Cui, D. Lin, Y. Li, Monitoring norepinephrine release in vivo using
1029 next-generation GRABNE sensors. *Neuron* **112**, 1930-1942.e6 (2024).
1030 113. T. V. P. Bliss, G. L. Collingridge, B.-K. Kaang, M. Zhuo, Synaptic plasticity in the anterior
1031 cingulate cortex in acute and chronic pain. *Nat Rev Neurosci* **17**, 485–496 (2016).
1032 114. M. Zhuo, Cortical excitation and chronic pain. *Trends Neurosci* **31**, 199–207 (2008).
1033 115. T. Kitamura, S. K. Ogawa, D. S. Roy, T. Okuyama, M. D. Morrissey, L. M. Smith, R. L.
1034 Redondo, S. Tonegawa, Engrams and circuits crucial for systems consolidation of a memory.
1035 *Science* **356**, 73–78 (2017).
1036 116. K. Yashiro, B. D. Philpot, Regulation of NMDA receptor subunit expression and its
1037 implications for LTD, LTP, and metaplasticity. *Neuropharmacology* **55**, 1081–1094 (2008).
1038 117. C. Lohmann, H. W. Kessels, The developmental stages of synaptic plasticity. *J Physiol*
1039 *(Lond)* **592**, 13–31 (2014).
1040 118. T. K. Hensch, Critical period regulation. *Annu Rev Neurosci* **27**, 549–579 (2004).
1041 119. K. He, M. Huertas, S. Z. Hong, X. Tie, J. W. Hell, H. Shouval, A. Kirkwood, Distinct
1042 eligibility traces for LTP and LTD in cortical synapses. *Neuron* **88**, 528–538 (2015).
1043 120. M. Inaba, T. Maruyama, Y. Yoshimura, H. Hosoi, Y. Komatsu, Facilitation of
1044 low-frequency stimulation-induced long-term potentiation by endogenous noradrenaline and
1045 serotonin in developing rat visual cortex. *Neurosci Res* **64**, 191–198 (2009).
1046 121. O. Flores, H. Pérez, L. Valladares, C. Morgan, A. Gatica, H. Burgos, R. Olivares, A.
1047 Hernández, Hidden prenatal malnutrition in the rat: role of β_1-adrenoceptors on synaptic
1048 plasticity in the frontal cortex. *J Neurochem* **119**, 314–323 (2011).
1049 122. T. Abel, P. V. Nguyen, M. Barad, T. A. S. Deuel, E. R. Kandel, R. Bourtchouladze, Genetic
1050 Demonstration of a Role for PKA in the Late Phase of LTP and in Hippocampus-Based
1051 Long-Term Memory. *Cell* **88**, 615–626 (1997).
1052 123. A. Govindarajan, I. Israely, S.-Y. Huang, S. Tonegawa, The dendritic branch is the
1053 preferred integrative unit for protein synthesis-dependent LTP. *Neuron* **69**, 132–146 (2011).
1054 124. Y. Chen, J. L. Saulnier, G. Yellen, B. L. Sabatini, A PKA activity sensor for quantitative
1055 analysis of endogenous GPCR signaling via 2-photon FRET-FLIM imaging. *Front. Pharmacol.*
1056 **5**, 56 (2014).
1057 125. X. Guirao, A. Kumar, J. Katz, M. Smith, E. Lin, C. Keogh, S. E. Calvano, S. F. Lowry,
1058 Catecholamines increase monocyte TNF receptors and inhibit TNF through beta
1059 2-adrenoreceptor activation. *Am J Physiol* **273**, E1203-8 (1997).
1060 126. D. Ağaç, L. D. Estrada, R. Maples, L. V. Hooper, J. D. Farrar, The β2-adrenergic receptor
1061 controls inflammation by driving rapid IL-10 secretion. *Brain Behav Immun* **74**, 176–185 (2018).
1062 127. R. B. Zinyama, G. J. Bancroft, L. B. Sigola, Adrenaline suppression of the macrophage
1063 nitric oxide response to lipopolysaccharide is associated with differential regulation of tumour
1064 necrosis factor-alpha and interleukin-10. *Immunology* **104**, 439–446 (2001).
1065 128. J. Deng, K. Muthu, R. Gamelli, R. Shankar, S. B. Jones, Adrenergic modulation of splenic

macrophage cytokine release in polymicrobial sepsis. *Am J Physiol, Cell Physiol* **287**, C730-6 (2004).

129. T. Yokoyama, S. Manita, H. Uwamori, M. Tajiri, I. Imayoshi, S. Yagishita, M. Murayama, K. Kitamura, M. Sakamoto, A multicolor suite for deciphering population coding of calcium and cAMP in vivo. *Nat. Methods* **21**, 897–907 (2024).

130. H. Pribiag, D. Stellwagen, TNF-α downregulates inhibitory neurotransmission through protein phosphatase 1-dependent trafficking of GABA(A) receptors. *J Neurosci* **33**, 15879–15893 (2013).

131. K. M. Tye, E. K. Miller, F. H. Taschbach, M. K. Benna, M. Rigotti, S. Fusi, Mixed selectivity: Cellular computations for complexity. *Neuron* **112**, 2289–2303 (2024).

132. S. Tazerart, D. E. Mitchell, S. Miranda-Rottmann, R. Araya, A spike-timing-dependent plasticity rule for dendritic spines. *Nat Commun* **11**, 4276 (2020).

133. E. Albarran, A. Raissi, O. Jáidar, C. J. Shatz, J. B. Ding, Enhancing motor learning by increasing the stability of newly formed dendritic spines in the motor cortex. *Neuron* **109**, 3298-3311.e4 (2021).

134. B. Basilico, L. Ferrucci, P. Ratano, M. T. Golia, A. Grimaldi, M. Rosito, V. Ferretti, I. Reverte, C. Sanchini, M. C. Marrone, M. Giubettini, V. D. Turris, D. Salerno, S. Garofalo, M.-K. St-Pierre, M. Carrier, M. Renzi, F. Pagani, B. Modi, M. Raspa, F. Scavizzi, C. T. Gross, S. Marinelli, M.-È. Tremblay, D. Caprioli, L. Maggi, C. Limatola, S. D. Angelantonio, D. Ragozzino, Microglia control glutamatergic synapses in the adult mouse hippocampus. *Glia* **70**, 173–195 (2022).

135. T. Paus, M. Keshavan, J. N. Giedd, Why do many psychiatric disorders emerge during adolescence? *Nat Rev Neurosci* **9**, 947–957 (2008).

136. V. Mondelli, A. C. Vernon, F. Turkheimer, P. Dazzan, C. M. Pariante, Brain microglia in psychiatric disorders. *Lancet Psychiatry* **4**, 563–572 (2017).

137. J. C. Grieger, V. W. Choi, R. J. Samulski, Production and characterization of adeno-associated viral vectors. *Nat Protoc* **1**, 1412–1428 (2006).

Figures

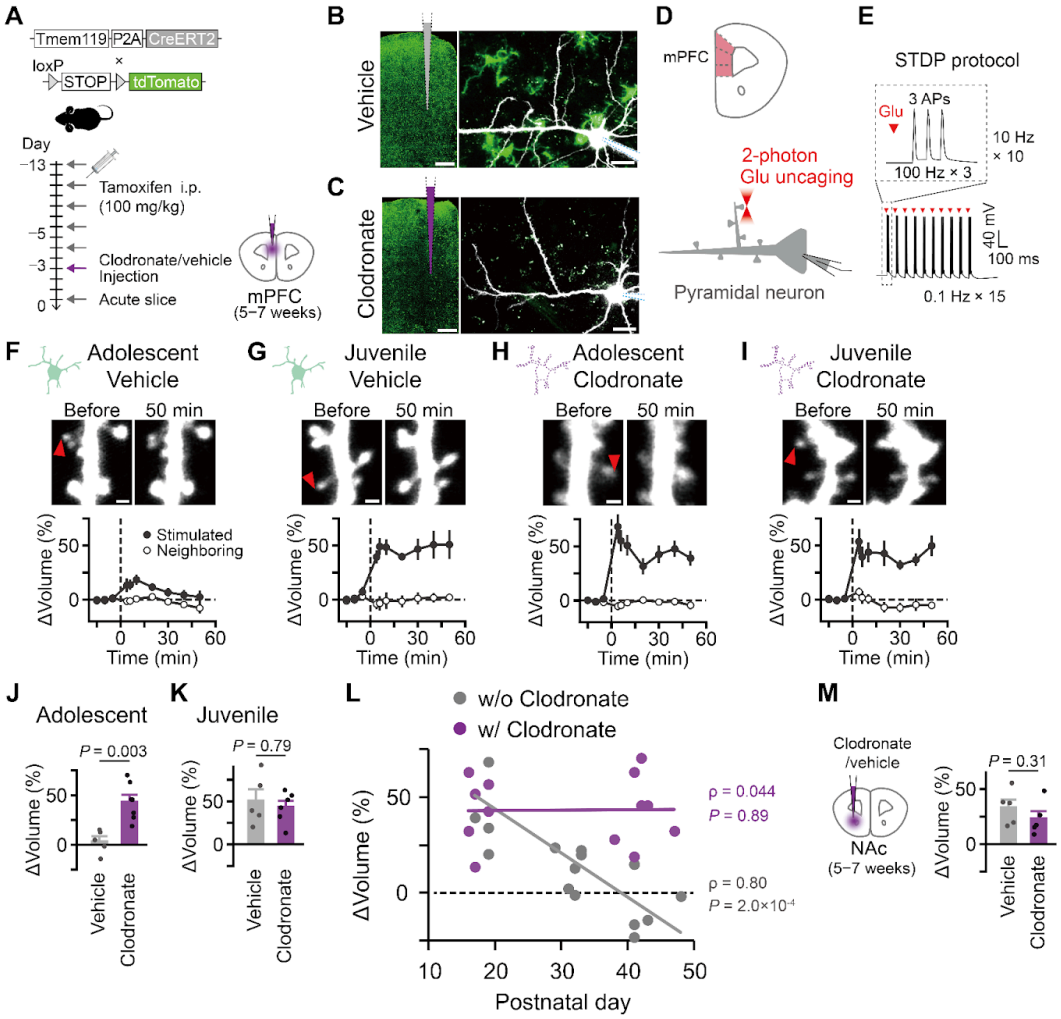

Figure 1. Microglial suppression of spine enlargement.
A, Schematic of a typical experimental timeline in adolescent (5–7 weeks old) transgenic mice.
B,C, Representative images of fixed slices with confocal microscopy (left) and acute slices with 2-photon microscopy (right) after vehicle (B) or clodronate (C) injections. Fluorescences of tdTomato for microglia (green) and Alexa 488 for neurons (white) are shown. Dotted lines indicate injection traces. Scale bars, 500 μm (left) and 20 μm (right).

D, Schematic of a brain slice containing the mPFC (top) and the experimental configuration for two-photon uncaging on dendritic spines of a pyramidal neuron (bottom). Caged-glutamate (CDNI-Glutamate, 4 mM) was applied using a puff pipette. Two-photon laser was directed to the tip of the spine head (720nm, 0.6 ms, 4−6 mW, adjusted depending on the depth of the dendrite). Small 3−4 spines located on the first to third branches of the apical dendrites (20 μm to 50 μm below the surface of the slice) were selected for plasticity induction. Glu, glutamate.
E, Schematic of the spike-timing-dependent plasticity (STDP) protocol. Each train consisted of 10 bursts (3 action potentials [APs] at 100 Hz) delivered at 10 Hz, where glutamate uncaging was paired with action potential within 10 ms. The train was repeated 15 times at 0.1 Hz.
F–I, Representative images of dendritic spines before and 50 minutes after STDP stimulation (top) and time courses of spine volume changes (bottom) in juvenile mice (2−3 weeks old) (F,H) and the adolescent mice (G, I) after vehicle (F, G) or clodronate (H, I) injections. Red arrows indicate stimulated spines. Scale bars, 1 μm.
J,K, Plots of spine volume changes. Volume changes were averaged over 40−50 minutes.
L, Plots of spine volume changes across ages. Statistical analysis was performed using Spearman's rank correlation coefficient test.
M, Schematic of clodronate injection into the nucleus accumbens (NAc) in adolescent mice (5–7 weeks old) (left) and plots of spine volume changes (right).
Error bars represent S.E.M. Mann–Whitney U test used for statistical analysis in (J,K,M).

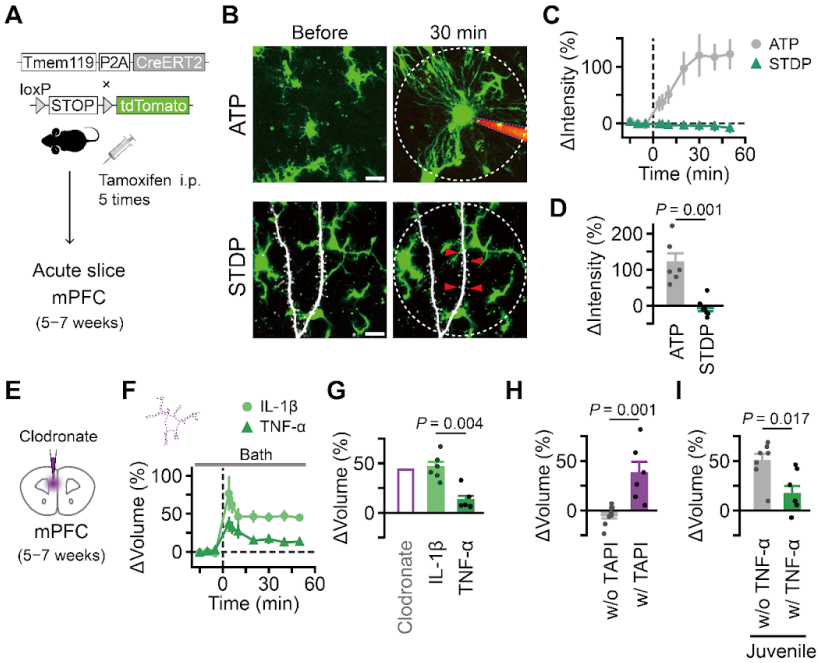

Figure 2. Signaling of microglial suppression.
A, Schematic of the experimental timeline.
B, Representative z-stack images (30 μm thick) of acute slices with 2-photon microscopy before (left) and after (right) ATP application from pipette (top) or STDP stimulation (bottom). Fluorescences of tdTomato for microglia (green), Alexa 488 for neurons (white), and Alexa 488 with 20 mM ATP in ACSF contained in the pipette (red) are shown. Red arrows indicate stimulated spines. White dotted circles denote the regions of interest (70 μm in diameter, centered at the ATP pipette tip or the stimulated spine area) for quantitative analyses. Scale bars, 10 μm.
C,D, Time courses (C) and plots (D) of changes in intensity in the regions of interest indicated in (B).
E, Schematic of clodronate injection.
F,G, Time courses (F) and plots (G) of spine volume changes in the slices with clodronate injections in the presence of IL-1β and TNF-α. The clodronate injection condition shown in (Figure 1J) is indicated as a reference.
H,I, Plots of spine volume changes following STDP stimulation in the absence and presence of TAPI-0 (TACE/ADAM17 inhibitor) (H) or in the absence and presence of TNF-α from juvenile mice (I). No clodronate injections were performed in these experiments.
Error bars represent S.E.M. Mann–Whitney U test used for statistical analysis in (D,G,H,I).

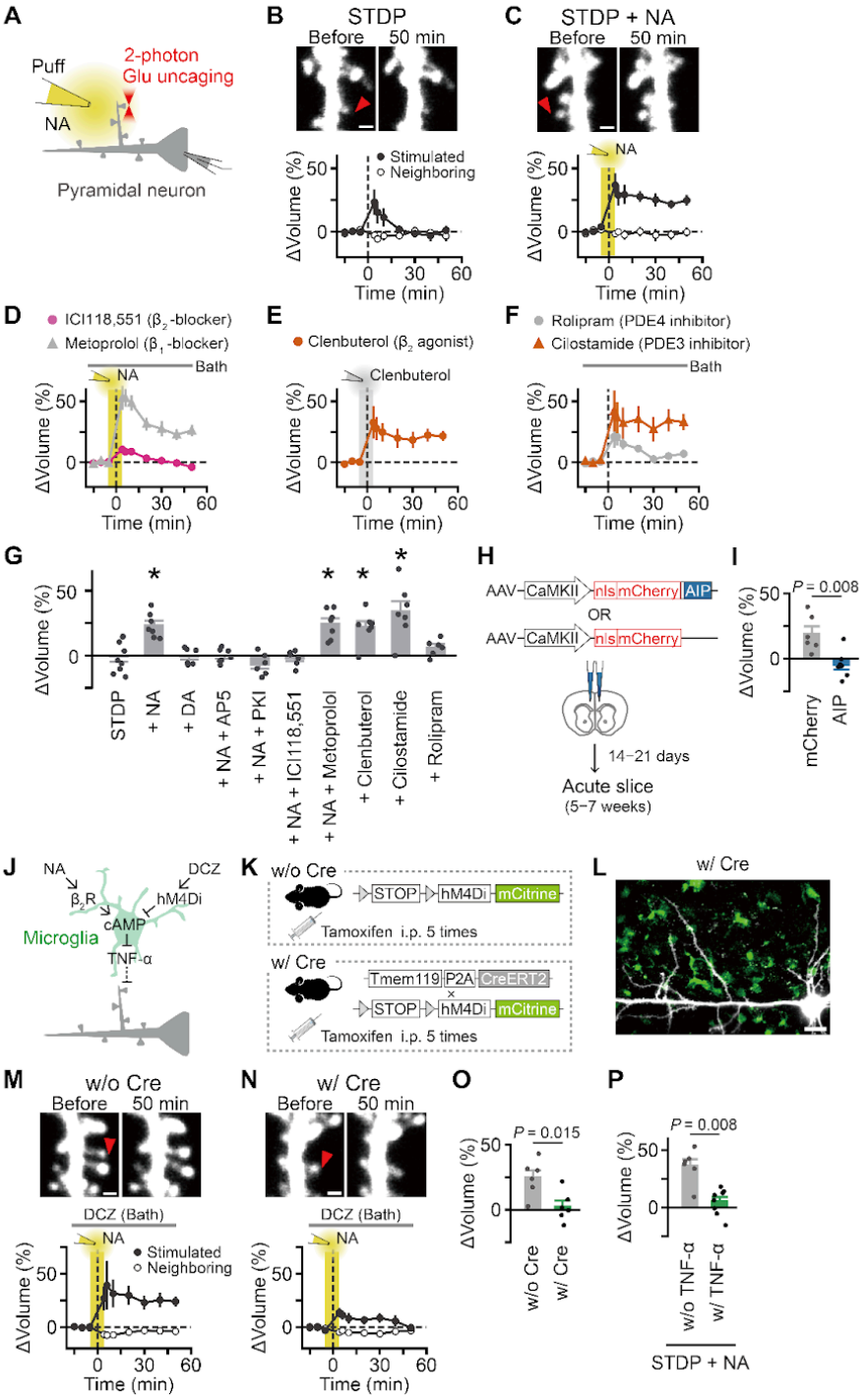
A
Puff
2-photon
Glu uncaging
NA
Pyramidal neuron
B
STDP
Before
50 min
Stimulated
Neighboring
ΔVolume (%)
Time (min)
C
STDP + NA
Before
50 min
NA
D
ICI118,551 (β2-blocker)
Metoprolol (β1-blocker)
Bath
E
Clenbuterol (β2 agonist)
Clenbuterol
F
Rolipram (PDE4 inhibitor)
Cilostamide (PDE3 inhibitor)
G
STDP
+ NA
+ DA
+ NA + AP5
+ NA + PKI
+ NA + ICI118,551
+ NA + Metoprolol
+ Clenbuterol
+ Cilostamide
+ Rolipram
H
AAV–CaMKII
nls mCherry
AIP
OR
14–21 days
Acute slice
(5–7 weeks)
I
P = 0.008
mCherry
AIP
J
NA
DCZ
β2R
hM4Di
cAMP
Microglia
TNF-α
K
w/o Cre
STOP
hM4Di
mCitrine
Tamoxifen i.p. 5 times
w/ Cre
Tmem119
P2A
CreERT2
L
w/ Cre
M
w/o Cre
DCZ (Bath)
N
w/ Cre
O
P = 0.015
w/o Cre
w/ Cre
P
P = 0.008
w/o TNF-α
w/ TNF-α
STDP + NA

Figure 3. Microglia-mediated noradrenaline actions on spine enlargement.
A, Schematic of the experimental configuration for puff application and two-photon uncaging on dendritic spines of a pyramidal neuron.
B,C, Representative images of dendritic spines before and 50 minutes after STDP stimulation (top) and time courses of spine volume changes after STDP stimulation (bottom) in the absence (B) and presence (C) of NA. Red arrows indicate stimulated spines. Shaded areas indicate the period of puff application. Scale bars, 1 μm.
D–F, Time courses of spine volume changes in the presence of β blockers with NA (D), β_2 agonist (E), and phosphodiesterase inhibitors (F). Gray shade and bars indicate the period of drug application.
G, Plots of spine volume changes. Volume changes were averaged over 40−50 minutes and subjected to statistical tests (Kruskal–Wallis test and post hoc Steel's test against STDP only). $^*P < 0.05$.
Error bars represent S.E.M.
H, Schematics of AAV vectors to express mCherry with or without AIP.
I, Plots of spine volume changes.
J, Schematic of a signaling model.
K, Schematic of R26-LSL-hM4Di-mCitrine mice without (w/o Cre) and with (w/ Cre) Tmem119-CreERT2 allele.
L, Image of an acute slice with 2-photon microscopy from a transgenic mouse (w/ Cre). Fluorescences of mCitrine (green) and Alexa 594 (white) are shown. Scale bar, 20 μm.
M,N, Representative images of dendritic spines before and 50 minutes after STDP stimulation (top) and time courses of spine volumes (bottom) in the slices without (M) and with (N) Cre. Gray bars indicate the period of DCZ (100 nM) application. Red arrows indicate stimulated spines. Scale bars, 1 μm.
O, Plots for spine volumes shown in (M,N).
P, Plots of spine volume changes in the absence and presence of TNF-α following STDP stimulation in the presence of NA from Supplementary Figure 6G.
Error bars represent S.E.M. Statistical analysis was performed using the Mann–Whitney U test in (F,G).

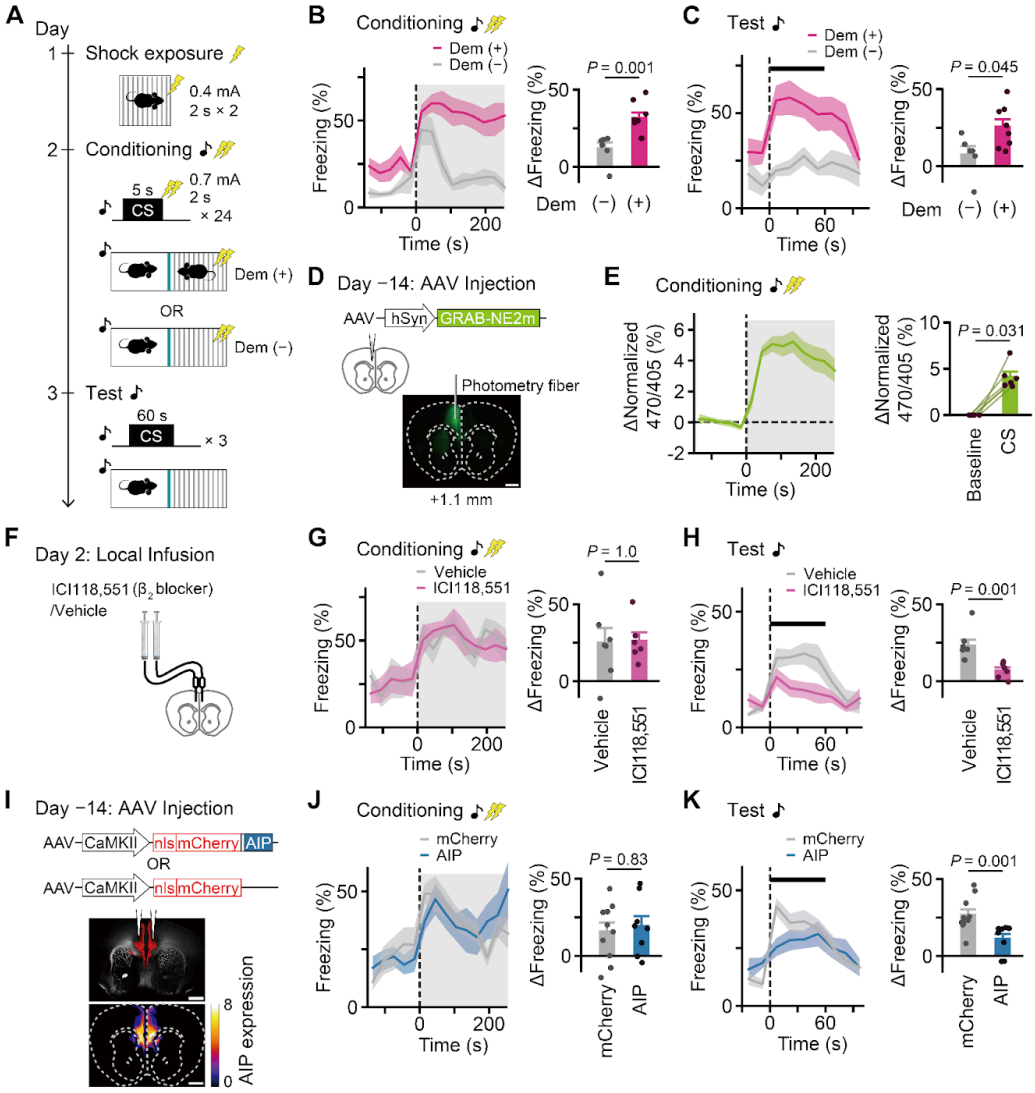

Figure 4. Noradrenaline and plasticity-related signaling in observational fear learning.

A, Schematic of the experimental timeline of observational fear learning.

B, Traces (left) and plots (right) of freezing on day 2. Grey shade indicates the conditioning period. The changes in freezing during the conditioning periods compared to the baseline periods on day 2 were plotted.

C, Traces (left) and plots (right) of freezing on day 3. Averaged freezing responses over the CS presentations are shown, and the bar indicates the CS period. The changes in freezing during the CS periods compared to the baseline periods on day 3 were plotted.

D, Schematic of the virus injection and fiber photometry experiment in the mPFC (top) and representative image showing fluorescence of GRAB-NE_{2m} (green) (bottom). The trace of fiber was overlaid on the image. Scale bar, 1 mm.

E, Traces (left) and plots (right) of GRAB-NE_{2m} fluorescence on day 2.
F, Schematic of cannula injection of ICI118,551 (β_2 inverse agonist). The experimental timeline of observational fear learning is the same as (A).
G, H, Traces and plots of freezing on day 2 (G) and on day 3 (H) in mice with injections of ACSF or ICI118,551 on day 2.
I, Images showing the spread of AIP expression. Representative (top) and the average of mCherry fluorescences after binarization from all the mice used in behavioral experiments (n = 8 mice) are shown. Scale bar, 1 mm.
J, K, Traces and plots of freezing on day 2 (J) and on day 3 (K) in mice injected with mCherry or AIP.
Mann–Whitney U test for (B, C, G, H, J, K). Wilcoxon signed-rank test for (E).
Error bars and shades indicate S.E.M.

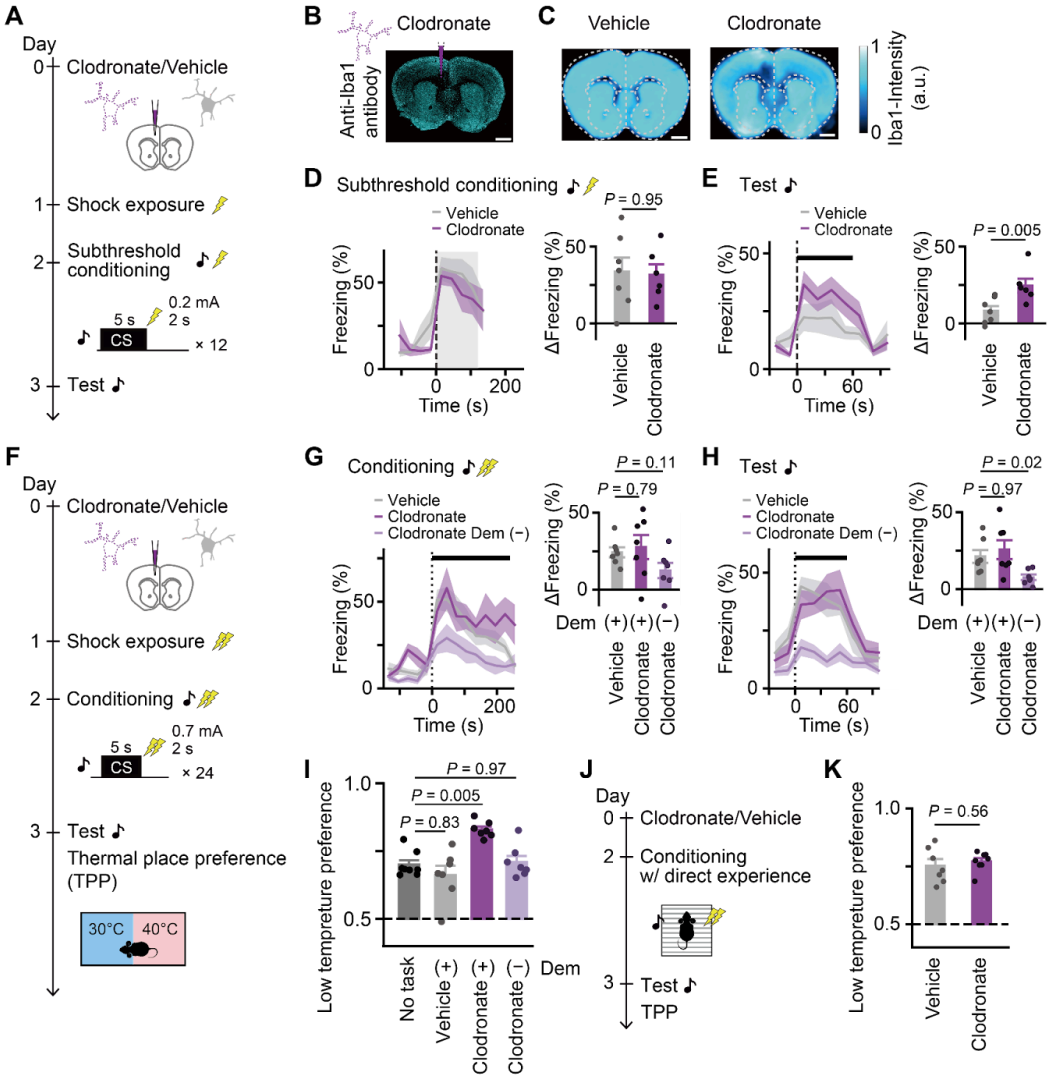

Figure 5. Microglial protection of cross-talk between emotional circuits.
A, Schematics of experimental timeline for subthreshold observational fear learning.
B, Representative image showing Iba1 immunoreactivity in clodronate injected brain. Scale bars, 1 mm.
C, Averaged images showing Iba1 immunoreactivity in the vehicle (left) and clodronate (right) injected brain. Averaged images were generated from all the brains used in behavioral experiments shown in (D) and (E). Dark color indicates areas with low Iba1 immunoreactivity. Scale bars, 1 mm.
D, E, Traces and plots of freezing on day 2 (D) and on day 3 (E) in mice with injections of vehicle or clodronate in subthreshold observational fear learning.
F, Schematic of experimental timeline for observational fear learning and subsequent thermal place preference test.

G, H, Traces and plots of freezing on day 2 (G) and on day 3 (H) in mice with injections of vehicle or clodronate in observational fear learning, and in mice with injections of clodronate without demonstrator.
I, Plots of thermal preference place after observational fear learning. Data for “No task” are the same as that shown in Supplementary Figure 9D.
J, Schematic experimental timeline for direct fear learning and subsequent thermal place preference test.
K, Plots of thermal place preference test after direct fear learning.
Error bars and shades indicate S.E.M.
Mann–Whitney U test for (D, E, K), Kruskal–Wallis test and post hoc Steel’s test for (G, H, I). P = 0.13, 0.0027, and 0.0027 for Kruskal–Wallis test in (G, H, I).

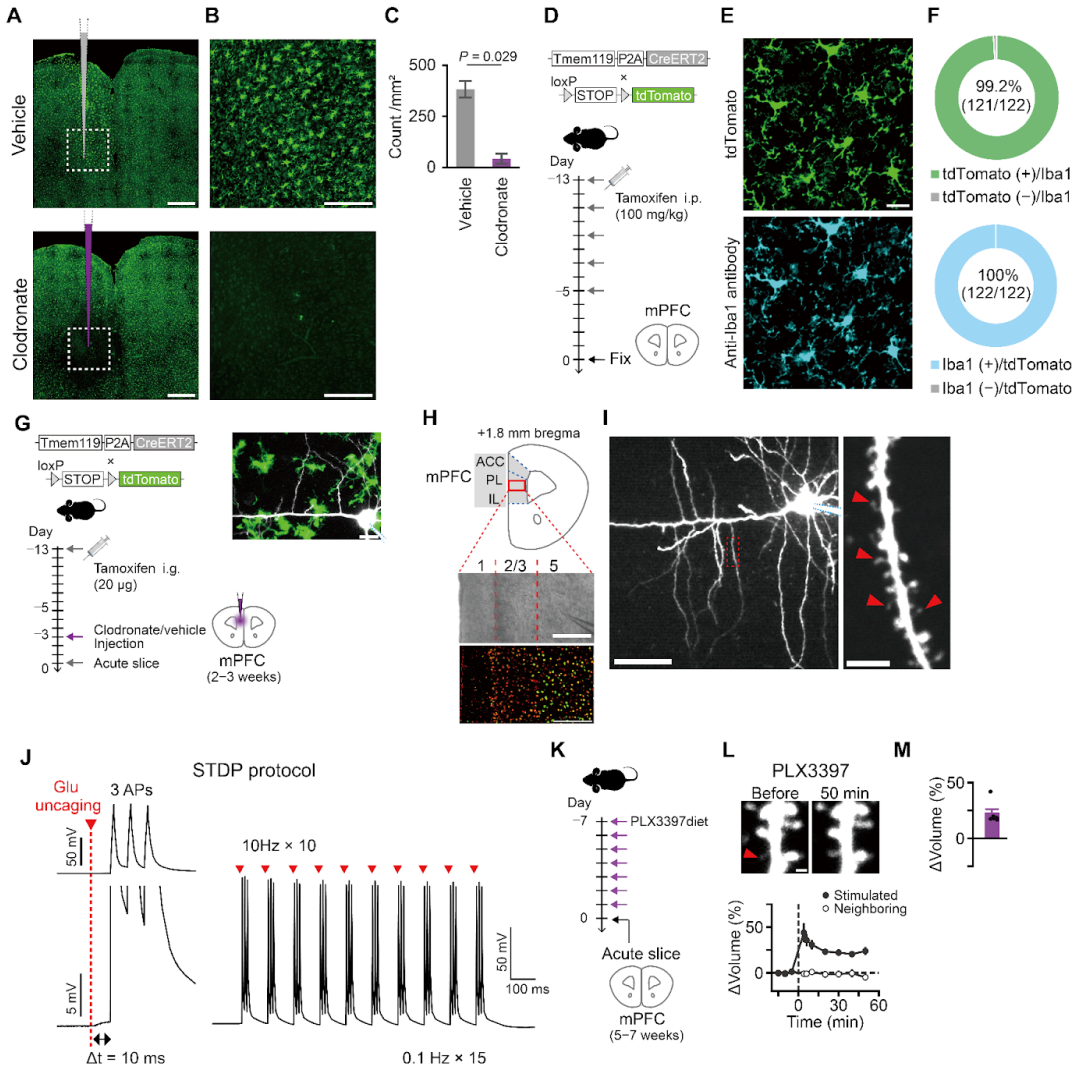

Supplementary Figure 1. Ablation of microglia and STDP stimulation.

A,B, Representative images of confocal microscopy showing anti-Iba1 fluorescence in low magnification (A) and high magnification (B) in brains 2 days after vehicle injection (top) and clodronate injection (bottom). Scale bars, 500 μm (A) and 200 μm (B). Dashed lines indicate the areas shown in high magnification.

C, Plots of microglial counts in the magnified areas shown in (A) and (B) 1–2 days after the injection. n = 4 mice per each condition. Mann–Whitney U test.

D, Schematic of the experimental timeline in transgenic mice.

E, Representative confocal microscopy images showing anti-Iba1 and tdTomato fluorescences. Scale bars, 20 μm.

F, Charts of cell counts from slices of 6 mice.

G, Schematic of the experimental timeline for microglial ablation in juvenile mice.

H, Schematics of a coronal slice containing the mPFC (top), and images showing electrode positioning (middle) and immunohistochemical labeling of cortical layers with Satb2 (red) and Ctip2 (green) (bottom). Neurons in the anterior cingulate cortex (ACC), prelimbic cortex (PL), or infralimbic cortex (IL) were recorded. Scale bars, 200 μm.
I, Images of a pyramidal neuron (left) and dendritic spines (right) obtained by 2-photon microscopy. Red arrows indicate typical spines stimulated by uncaging. Scale bars, 50 μm (left) and 5 μm (right).
J, Traces of membrane potential during one burst (left) and one train (right) of stimulation in STDP protocols. Action potentials (APs) were evoked by pulsed current injections (1.5−2.0 nA, 2 ms).
K, Schematic of experimental timeline. adolescent mice were fed PLX3397 containing chow (100 mg/kg of chow) for 7 days.
L, Representative images of dendrites before and 50 minutes after STDP stimulation (top) and time courses of spine volumes (bottom). Red arrows indicate stimulated spines. Scale bars, 1 μm.
M, Plots of spine volume changes.
Error bars represent S.E.M.

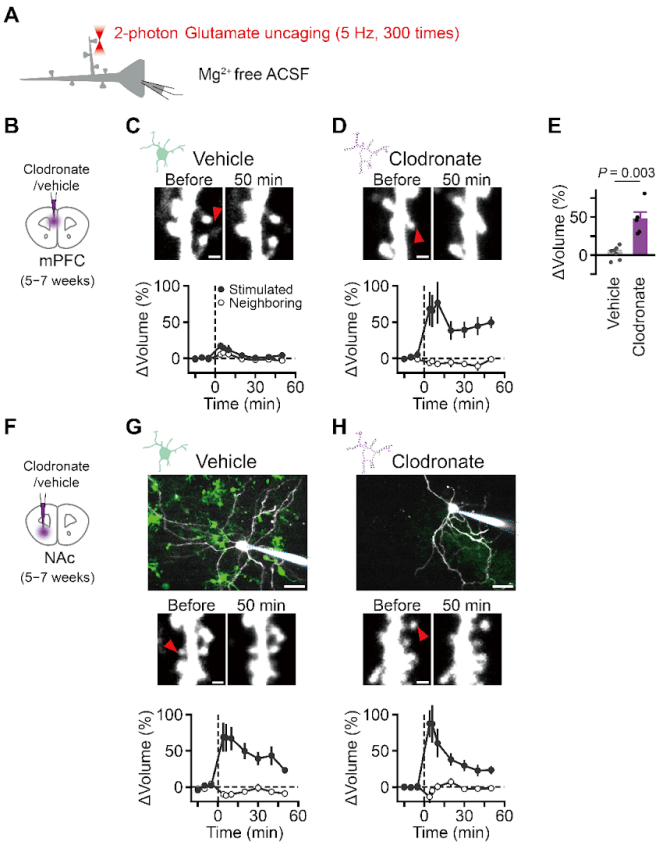

Supplementary Figure 2. Spine enlargement in magnesium-free condition.
A, Schematic of the experimental configuration for two-photon uncaging on dendritic spines of a pyramidal neuron under Mg^{2+}-free conditions. Whole-cell recordings were made to confirm uncaging-induced EPSCs, but action potentials were omitted during plasticity induction.
B, Schematic of clodronate or vehicle injection in adolescent mice (5−7 weeks old).
C,D, Representative images of dendrites before and 50 minutes after STDP stimulation (top) and time courses of spine volumes (bottom) in the slices with vehicle (C) and clodronate (D) injections. Scale bars, 1 μm.
E, Plots of spine volume changes.
F, Similar to (B) but injections and experiments were performed in the nucleus accumbens (NAc).
G,H, Representative images of acute slices in the NAc from Tmem119-CreERT2; Ai14 mice (top) and dendrites before and 50 minutes after STDP stimulation (middle) and time courses of spine volumes (bottom) in the slices with vehicle (G) and clodronate (H) injections. Scale bars, 20 μm (top) and 1 μm (middle).
Error bars represent S.E.M.

Red arrows indicate stimulated spines.
Statistical analysis was performed using the Mann–Whitney U test in (E).

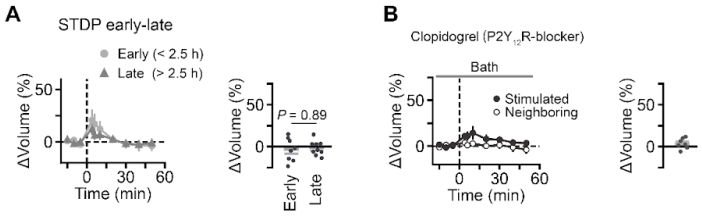

Supplementary Figure 3. Effects of acute slice preparation.
A, Time courses of spine volumes before and after 2.5 hours of slice preparation (left) and plots of spine volume changes (right). Data from Figure 1F and Figure 3B were reanalyzed. Incubation times at the time of STDP stimulation were 2.4 ± 0.2 h and 4.5 ± 0.9 h (mean ± SD), respectively. Statistical analysis was performed using the Mann–Whitney U test.
B, Time courses of spine volumes (left) and plots of spine volume changes (right) in the presence of Clopidogrel (10 μM, $P2Y_{12}$ receptor antagonist). Gray bars indicate the periods for bath application.

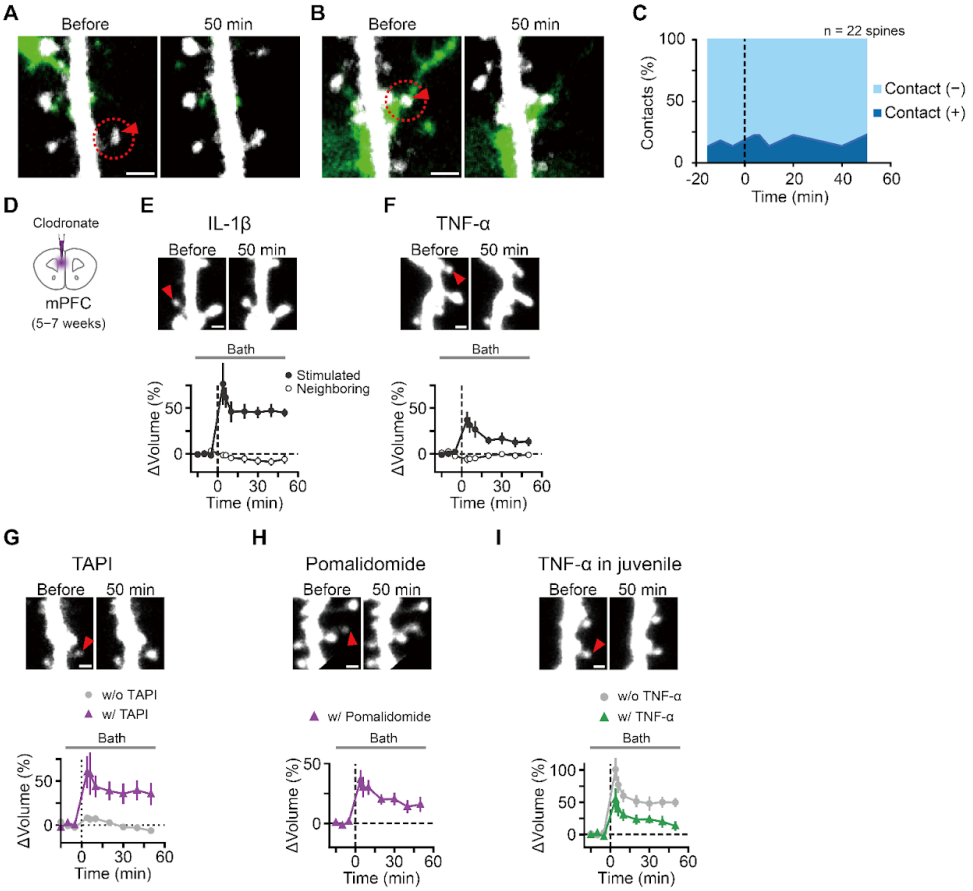

Supplementary Figure 4. Microglial downstream signaling.

A, Representative images showing the absence of microglia (green) near the stimulated spine before and after STDP stimulation. The absence of contact was defined by the lack of green signal (within 3 S.D. of a reference background area) in the regions-of-interest (red dashed circle, 4 μm in diameter centered on the stimulated spine) in the 4 μm z-stack image.

B, Representative images of microglia located near the stimulated spine.

C, Plots showing the proportion of microglial contacts with stimulated spines over time.

D, Schematic of clodronate injection in adolescent mice (5−7 week old).

E,F, Representative images of dendrites before and 50 minutes after stimulation (top) and plots of spine volumes (bottom) in the slices with clodronate injections in the presence of IL-1β (1 ng/ml, bath) (E) and TNF-α (10 nM, bath) (F).

G, H, Representative images and plots of spine volume changes in the presence of the TAPI-0 (1 μM, bath) (G) and Pomalidomide (100 μM, bath, TNF-α receptor inhibitor) (H) in adolescent mice.

I, Representative images and plots of spine volume changes in the presence of TNF-α (10 nM, bath) in juvenile mice (2−3 weeks old).

Red arrows indicate stimulated spines. Scale bars, 2 μm in (A, B), 1 μm in (E, F, G, H, I). Error bars represent S.E.M.

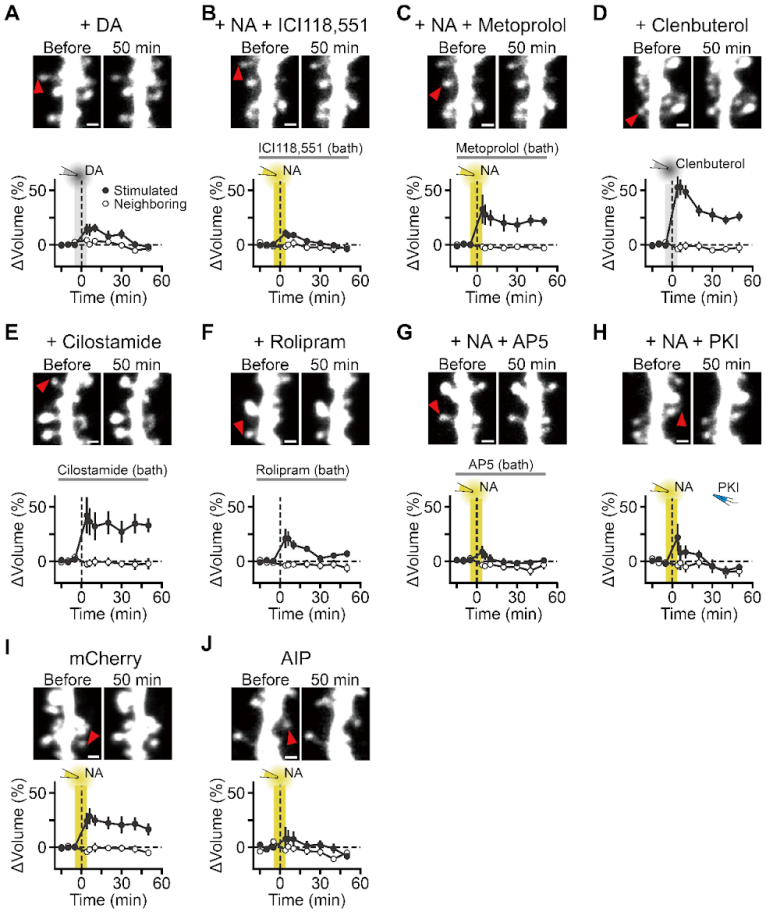

Supplementary Figure 5. Pharmacological studies on spine enlargement in the mPFC.

A–**H,** Representative images of dendrites before and 50 minutes after stimulation (top) and time courses of spine volumes after STDP stimulation (bottom) in the presence of (A) dopamine (DA), (B) NA and a β_2 blocker, (C) NA and a β_1 blocker, (D) a β_2 agonist, (E) PDE3 inhibitor, (F) PDE4 inhibitor, (G) NA and AP5, and (H) NA and PKI. Shading indicates the periods of puff application for DA, NA or a β_2 agonist. Gray bars indicate the periods for bath application. Error bars represent standard error. Filled and open symbols represent spine volumes measured from stimulated spines and unstimulated neighboring spines (control), respectively. Red arrows indicate stimulated spines.

I, J, Representative images of dendrites before and 50 minutes after stimulation (top) and time courses of spine volumes (bottom) in the absence (I) and presence (J) of AIP. Scale bars, 1 μm. Error bars represent S.E.M.

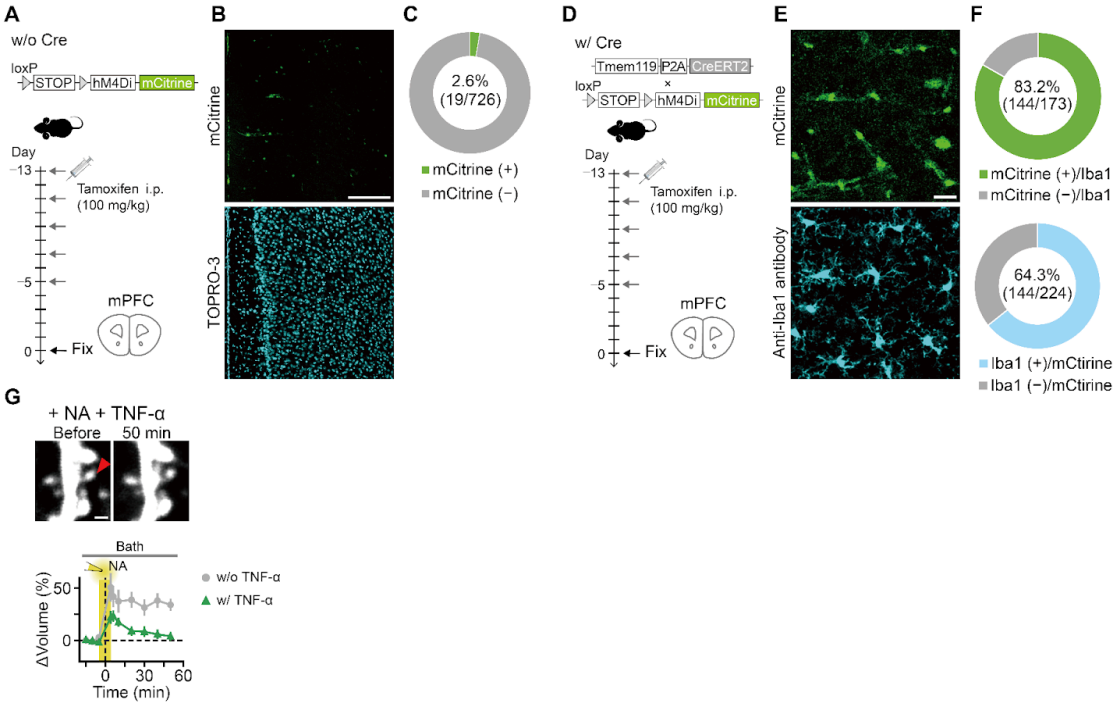

Supplementary Figure 6. Chemogenetic manipulation of microglia.
A, Schematic of the experimental timeline in mice without the Cre-driver.
B, Images showing mCitrine fluorescence (top) and nuclear staining with TOPRO-3 (bottom) in mice without the Cre-driver.
C, Chart showing proportion of mCitrine expressing cells out of TOPRO-3 positive cells. Data were obtained from slices of 2 mice.
D, Schematic of experimental timeline in mice with Cre-driver.
E, Images showing mCitrine fluorescence (top) and immunostaining with anti-Iba1 antibody (bottom) in mice with Cre-driver.
F, Chart showing proportion of the mCitrine expressing cells out of anti-Iba1 positive cells (top) and anti-Iba1 positive cells out of mCitrine expressing cells (bottom). Slices from 6 mice.
G, Representative images of dendrites before and 50 minutes after STDP stimulation (top) and time courses of spine volumes (bottom) with or without TNF-α (10 nM, bath) in the presence of NA (50 μM). Red arrows indicate stimulated spines.
Scale bars, 200 μm in (B), 20 μm in (E), and 1 μm in (G).
Error bars represent S.E.M.

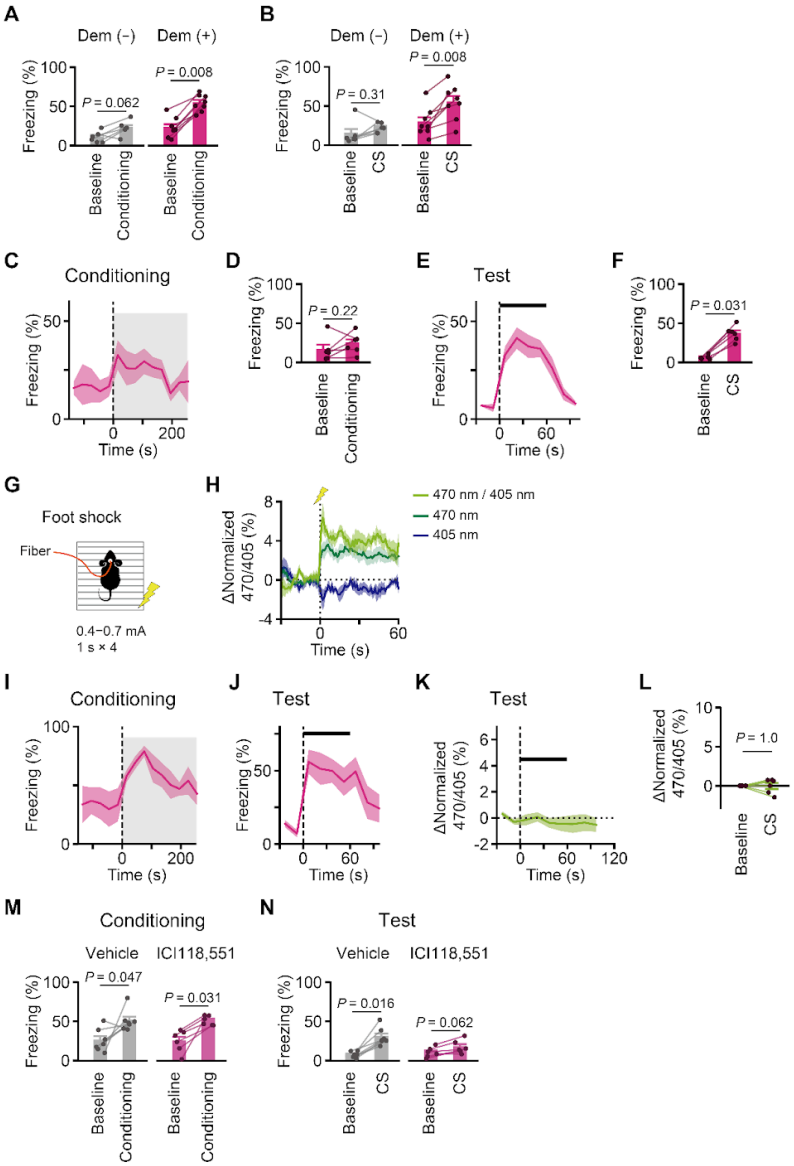

Supplementary Figure 7. Observational fear learning.
A, B, Plots of freezing on day 2 of conditioning (A) and day 3 of test (B) of mice conditioned with or without demonstrator.
C−F, Traces (C,E) and plots (D,F) of freezing on day 2 of conditioning (C,D) and day 3 of test (E,F) in female mice. A pair of female mice was used for observer and demonstrator.
G, Schematic of photometry recording in response to foot shock (0.4−0.7mA, 1 s).
H, Traces of raw fluorescences (signals obtained by excitation with 405 nm LED or 470 nm LED) and ratio (470 nm/405 nm) against the onset of the foot shock. Averages of 4 trials are shown. Note that the isosbestic wavelength of the probe is around 410 nm and

therefore the signal with 405 nm excitation exhibited the opposite direction to that of 470 nm excitation. These mice were a separate set from those used in observational fear learning.

I,J, Traces of freezing on day 2 (I) and day 3 (J) in fiber photometry recording experiment.

K,L, Trace (K) and plots (L) of GRAB-NE_{2m} fluorescence on day 3.

M,N, Plots of freezing on day 2 (M) and on day 3 (N) in ICI118,551 experiments.

Wilcoxon signed-rank test for (A, B, D, F, L, M, N).

Error bars and shades indicate S.E.M.

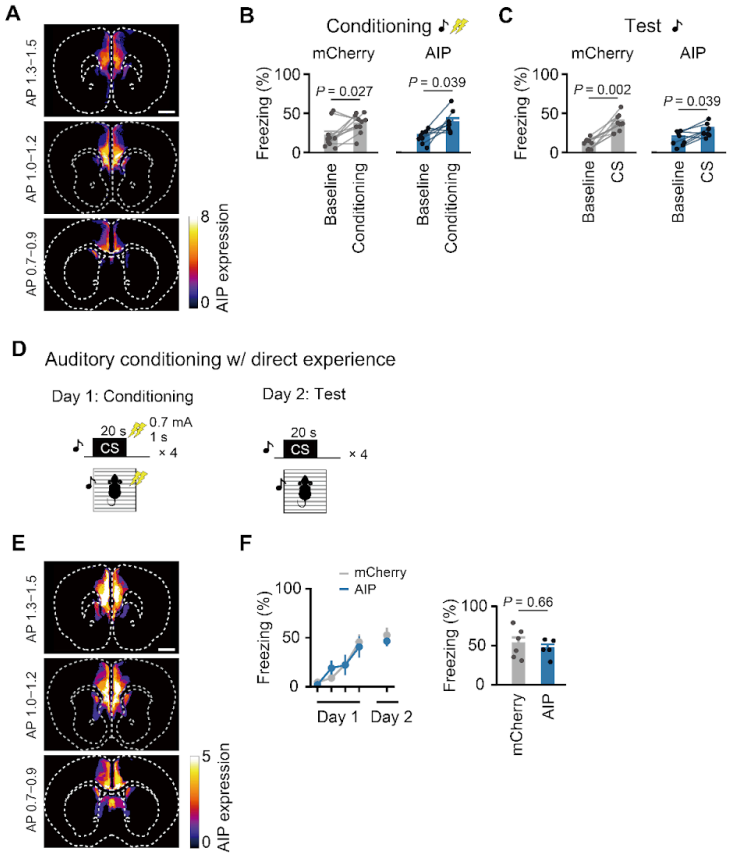

Supplementary Figure 8. Inhibition of CaMKII signaling in fear learning.
A, Images showing averaged intensity of AIP expression in all the mice engaged in the observational fear learning. AP indicates anteroposterior coordinates from the bregma in mm.
B, C, Plots of freezing on day 2 (B) and on day 3 (C) in AIP experiments.
D, Schematic of auditory conditioning with direct fear experience.
E, Images showing averaged intensity of AIP expression in all the mice engaged in auditory conditioning with direct fear experience.
F, Time courses of freezing on day 1 (conditioning) and on day 2 (test) (left) and plots on day 2 (right). Freezing responses during tone periods (20 s) are shown for each trial (day 1) or average of 4 trials (day 2).
Scale bars in (A, E) indicate 1 mm.
Wilcoxon signed-rank test for (B,C), Mann–Whitney U test for (F).

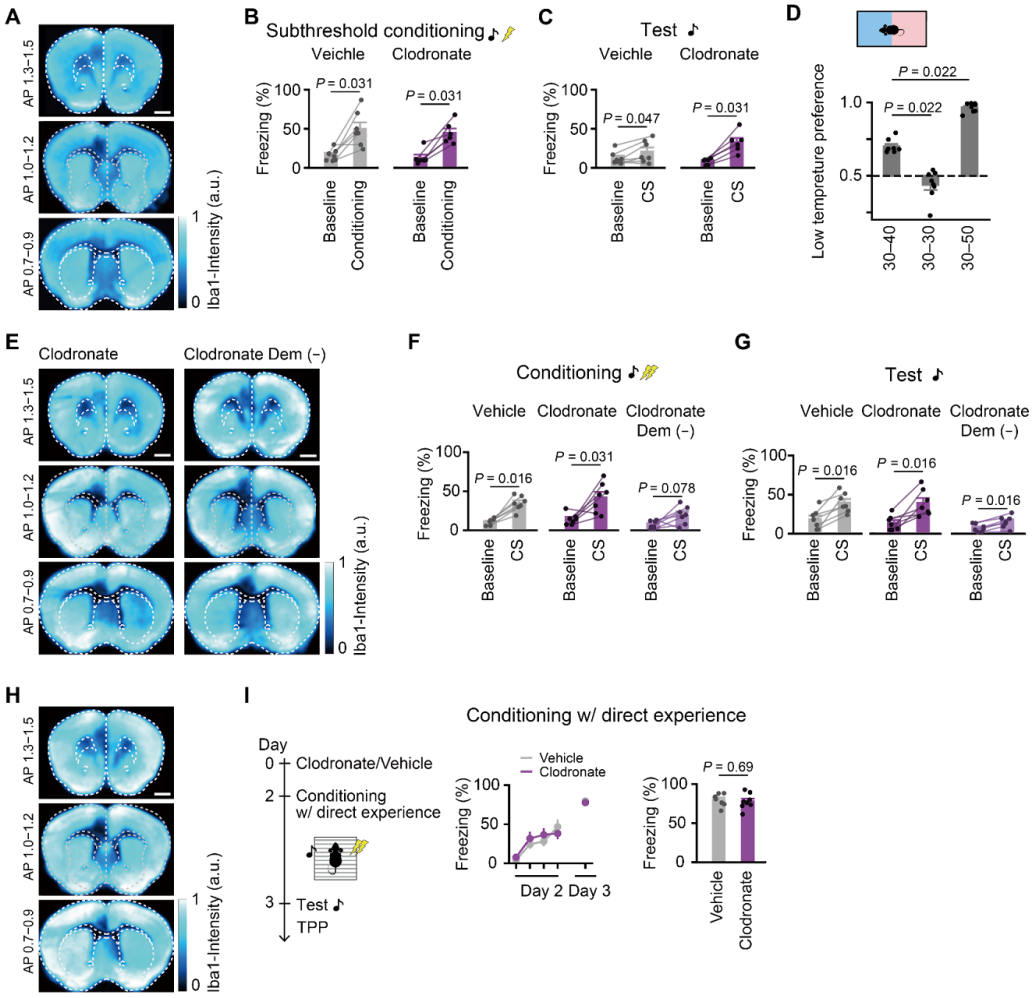

Supplementary Figure 9. Ablation of microglia in fear learning.
A, Images showing averaged intensity of Iba1 immunoreactivity in the brain from all the clodronate-injected mice used for subthreshold conditioning.
B,C, Plots of freezing on day 2 (B) and on day 3 (C) in subthreshold conditioning.
D, Thermal place preference with various temperatures. Times spent in the lower temperature plate during the latter 5 min out of total 10 min recording periods are shown**.**
E, Images of Iba1 immunoreactivity from all the mice used for conditioning and thermal place preference test.
F, G, Plots of freezing on day 2 (F) and on day 3 (G) in conditioning with clodronate injections with and without demonstrator.
H, Images of Iba1 immunoreactivity from all the mice used for conditioning with direct experience.
I, Auditory fear conditioning with direct experience in the presence and absence of

clodronate.
Scale bars in (A, E, H) indicate 1 mm. Wilcoxon signed-rank test for (B,C, F, G), Wilcoxon signed-rank test with Bonferroni correction after Friedman test ($P < 0.001$) for (D), Mann–Whitney U test for (I).

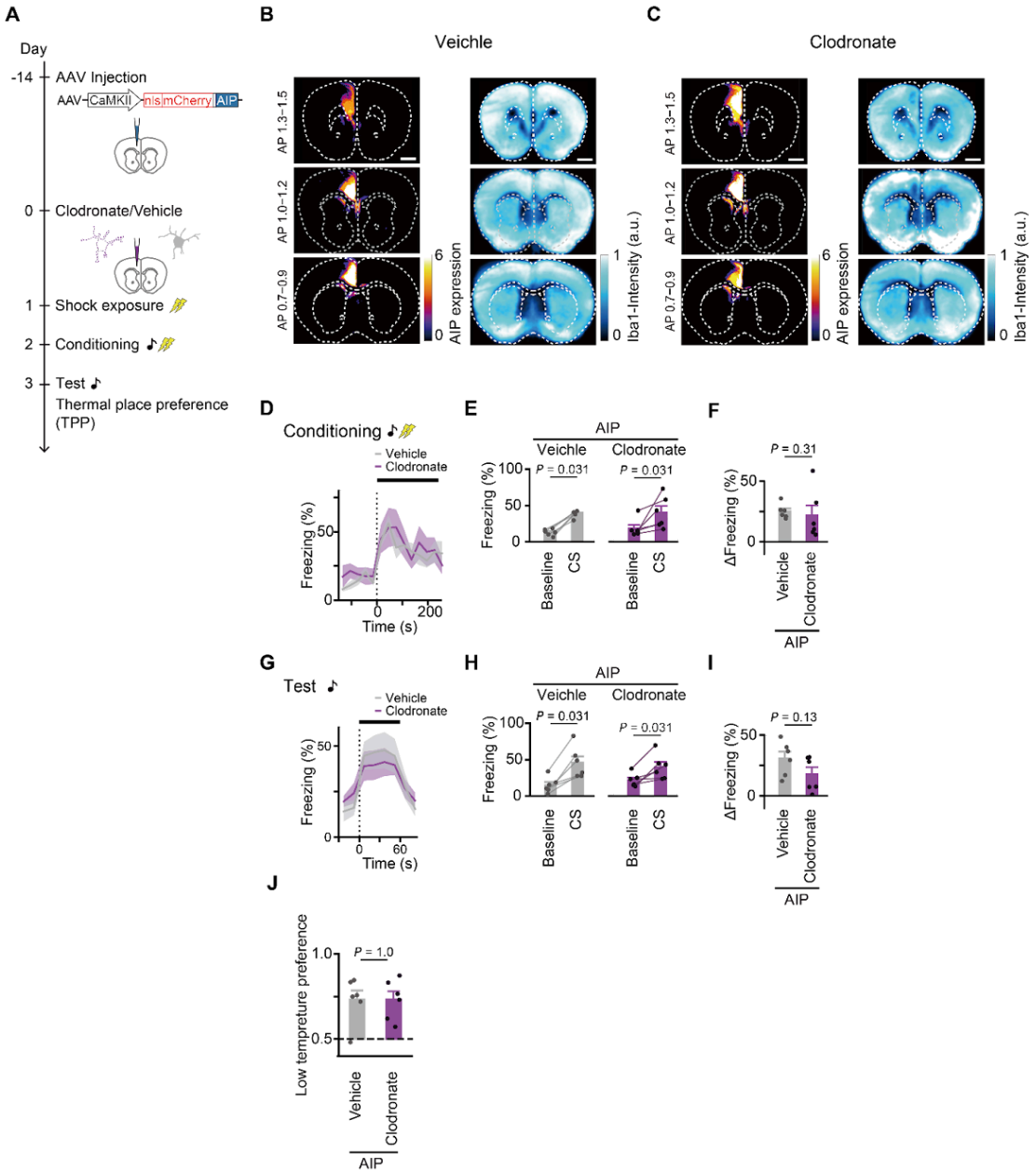

Supplementary Figure 10. Occlusion of microglial ablation effects on thermal sensitivity.

A, Schematic diagram for experimental timeline. The procedure is the same as in Figure 5F, except that mice were injected with AIP-expressing AAV in the right mPFC.

B,C, Images showing averaged AIP expression intensity (left) and Iba1 immunoreactivity (right) in the brain from all mice engaged in the task with vehicle (B) and clodronate (C) injections.

D−I, Traces and plots of freezing on day 2 (D, E, F) and on day 3 (G, H, I).

J, Plots of thermal place preference**.**
Wilcoxon signed-rank test for (E, H), Mann–Whitney U test for (F, I, J).